Remote Sensing of Environment 298 (2023) 113822

Contents lists available at ScienceDirect

Remote Sensing of Environment

journal homepage: www.elsevier.com/locate/rse

# An evaluation of the NOAA global daily gap-filled VIIRS surface albedo

Jingjing Peng [a,*], Peng Yu [a,b], Yunyue Yu [b], Aolin Jia [a], Dongdong Wang [a], Heshun Wang [a], Zhihao Wang [a]

[a] Earth System Science Interdisciplinary Center/ Cooperative Institute for Satellite Earth System Studies (CISESS), University of Maryland, College Park, MD 20740, USA

[b] NOAA NESDIS Center for Satellite Applications and Research, College Park, MD 20740, USA

ARTICLE INFO

Edited by Jing M. Chen

*Keywords:*
Albedo
VIIRS
JPSS
S-NPP
NOAA-20
Radiation budget

ABSTRACT

The land surface albedo product of visible infrared imaging radiometer suite (VIIRS) in National Oceanic and Atmospheric Administration (NOAA)'s operational system provides real-time, global daily mean surface albedo, which is a required parameter in the estimation of the daily shortwave net radiation budget. The global gridded VIIRS albedo product is derived from the level-2 granule surface albedo product, which is generated using a Direct Estimation Method. Special gridding and compositing algorithms were developed for aggregating the granular albedo data into the gridded albedo product. This paper describes the design and evaluation of the NOAA VIIRS gridded daily surface albedo product. The cloudy condition, retrieval path, retrieval method, and observing geometry are the criteria in deciding the priority order in the composition processing. The proposed albedo product possesses a complete spatial coverage over global land and ice surface and provides a timely response to surface dynamics. The validation of satellite retrieved daily mean albedo against ground counterparts over a series of well-maintained networks demonstrates the reliability of the composed albedo considering the interference of the seasonal surface heterogeneity conditions around each site. The inter-comparison between the S-NPP and NOAA-20 VIIRS albedo shows good agreement, except for a minor bias related to solar/view angle differences. The cross-comparison between VIIRS albedo and MODIS albedo shows good consistency with some deviations related to the controversy between their upstream snow mask.

## 1. Introduction

Surface albedo determines the amount of shortwave energy reflected upward at the surface; thus, it determines the net shortwave radiation budget at the surface. Albedo is defined as one of the essential climate variables by the global climate observing system (GCOS) as it affects climate change through various mechanisms (Liang et al., 2019; Chapin et al., 2008). Examples include the global warming impact induced through albedo change from anthropogenic land use change (Pitman et al., 2011; Abraha et al., 2021), the cooling effect of boreal deforestation (Alkama and Cescatti, 2016; Lee et al., 2011), substantial contribution of altered snow/ice albedo to recent high-latitude warming trends (Gleeson et al., 2014; Chapin et al., 2005), and feedback of albedo to drought conditions in North Africa (Knorr and Schnitzler, 2006; Kucharski et al., 2013) and Sahel (Zhou et al., 2007). Kumar et al. Kumar et al. (2020) has observed the impact of snow albedo on the snow accumulation and melt time by assimilating the Global Land-Surface Satellite (GLASS) albedo within the Noah multi-parameterization (Noah-MP) land surface model. This further demonstrates how satellite albedo products could be utilized in understanding and predicting changes in the Earth's environment.

Satellite albedo products (Qu et al., 2015) furnish globally available moderate-resolution albedo estimations in near-real-time frequencies, utilizing instruments like the Moderate Resolution Imaging Spectroradiometer (MODIS) (Schaaf et al., 2002) and the visible infrared imaging radiometer suite (VIIRS) (Wang et al., 2013), or as earth science data record, such as GLASS (Qu et al., 2013) and CLARA (Riihelä et al., 2013). Broadband albedo (i.e., the albedo that characterizes the entire solar spectrum) can be estimated via spectral extrapolation from spectral albedos based on their empirical relationships, that is, a narrowband-to-broadband (NTB) conversion (Greuell and Oerlemans, 2004; Liang, 2001). The NASA MODIS albedo algorithm Ambrals (Algorithm for MODIS bidirectional reflectance anisotropy of the land surface) (Schaaf et al., 2002), which is a common method, applies NTB conversion to hemispherical surface reflectance derived from the parameter modeling and hemispherical integration of the

* Corresponding author.
*E-mail address:* jjpeng@umd.edu (J. Peng).

https://doi.org/10.1016/j.rse.2023.113822
Received 26 May 2022; Received in revised form 11 September 2023; Accepted 14 September 2023
Available online 27 September 2023

surface bidirectional reflectance distribution function (BRDF) (Lucht, 1998; Lucht and Roujean, 2000). The NTB conversion relationship provides the average weighting function due to downward flux distribution at the bottom of the atmosphere. It is approximated as a linear relationship regressed from representative samples of surface types and atmospheric conditions. Although proved efficient when the clear-sky multi-angle observations is sufficiently sampled during a period to retrieve BRDF coefficients (Liu et al., 2009a; Jin et al., 2003; Stroeve et al., 2013; Wang et al., 2012b, 2014; Song et al., 2019), the Ambrals method suffers from data gaps when continuous cloud coverage dominates. An alternative, called the Direct Estimation Method hereinafter (Schaepman-Strub et al., 2006), is to regress the broadband surface albedo from the top-of-atmosphere (TOA) spectral reflectance, strictly referred to as the hemispherical–directional reflectance factor. The statistical coefficients combine the conversion relationships, including atmospheric correction, anisotropy correction, and spectral correlations. The coefficients are refined according to the solar-view-geometry of the TOA reflectance with consideration of the surface type.

This Direct Estimation Method has been applied in operational albedo products, such as GLASS and VIIRS. GLASS albedo has been determined to have similar accuracy to the MODIS albedo product (Liu et al., 2013b) and has been applied in numerical data assimilation owing to its gap-free feature (Kumar et al., 2020). It provides a long-term historical gridded albedo dataset with 8-day temporal resolution. In contrast, the VIIRS albedo environment data record (EDR) provides a near-real-time daily mean albedo estimation with a latency of no more than 5 h after the creation of the sensor data record (SDR). This is a granule (Hillger et al., 2022) product at a nominal pixel spatial resolution of 750 m. The VIIRS algorithm uses a Direct Estimation Method owing to its feasibility and efficiency as it relies on a single observation (Wang et al., 2017). The earlier interface data processing segment (IDPS) version of the VIIRS albedo EDR, operational from 2014 through 2019, provides instantaneous blue-sky-albedo, that is, the albedo measured under natural outdoor illumination (including direct solar radiation and diffuse sky irradiance) at the overpass time only over clear-sky pixels with the cloudy pixel value invalid. Many validation attempts have confirmed the validity of the VIIRS albedo EDR although regression varies with surface type (Wu et al., 2017; Zhou et al., 2016; Justice et al., 2013). A larger noise in desert albedo retrieval was reported based on the comparison with in-situ measurements (Justice et al., 2013). The application of a single BRDF for bare soil and snow surfaces has determined the inherent uncertainty in the result generated from a generic look-up table (LUT). LUTs that are specific for bare soil and snow have been added through regression from separate samples combined with the corresponding aerosol optical depth (AOD) types (Wang et al., 2017). Zhou et al. (2016) demonstrated a much improved performance resulting from the application of LUTs that are specific to bare soil and snow. Wu et al. Wu et al. (2017) confirmed the distinct advantages of VIIRS albedo against its GLASS and MODIS counterparts in terms of temporal continuity and the ability to capture abrupt changes in surface albedo, especially over mixed-cover surfaces.

The IDPS VIIRS albedo EDR only represents the instantaneous condition at satellite overpass and restricts its application in energy balance where daily mean albedo is desired (Grant et al., 2000). Surface albedo shows the diurnal change with the variation of illumination conditions (Grant et al., 2000; Jacob and Olioso, 2005) under the changing solar zenith angle and atmospheric parameters (e.g.,transmissivity), surface type, and surface condition (e.g.,moisture) (Minnis et al., 1997). The new Enterprise VIIRS albedo EDR, from the Enterprise Processing System (EPS), provides the daily mean albedo, rather than instantaneous albedo. Daily mean albedo here refers to daily mean broadband blue-sky surface albedo, which could be calculated from integrals of instantaneous upwelling shortwave radiation and incident shortwave radiation (Wang et al., 2017). Moreover, the Enterprise VIIRS albedo improved in its coverage by providing gap-free granular albedo EDR over all-sky conditions. The cloudy-sky albedo is estimated through temporal filtering from preceding observations and prior calculated albedo climatology (Jia et al., 2022). Additionally, to satisfy the unprecedented demand for authoritative information on sea-ice albedo, VIIRS albedo granules also provide shortwave daily mean albedo over sea-ice surface; the results suggest high reliability through different seasons based on validation with ground measurements (Peng et al., 2018).

However, the top remaining challenge in applying the L2 albedo EDR is the mapping from granule-specific geolocation data. Although the level-2 (L2) granule albedo product maintains the observing geometry and spatial range of the raw satellite feed, users cannot easily subset data over an area of interest. Then, more than one retrievals may be generated for the same location due to repeat satellite visits within a single day, with higher likelihood at higher latitude. The overlapped observations may cause confusion for modelers who require only gridded daily albedo products. The subsequent main issue in the generation of the daily gridded albedo product is selecting the most representative retrievals from repeat observations considering the varying cloud condition, solar/view zenith angles, and surface cover types. The strategy about the VIIRS level-3 (L3) albedo algorithm, which generates a global gap-free gridded albedo product from the L2 granule albedo, is introduced in Section 2.3. This paper is organized as follows. Section 2 provides the details of the data and methods. The L2 algorithm narration in Section 2.2 provides background of how daily mean albedo is derived using the Direct Estimation Method. The L3 algorithm, as introduced in Section 2.3, was implemented with two processing steps: anchoring the science data to specific geographic points and generating the optimal albedo map out of multiple layers from different observations within a day. Comparable daily mean albedos were obtained from in-situ measurements (details in Section 2.4) and MODIS BRDF products (details in Section 2.5) to provide a reference value for the VIIRS albedo evaluation. Section 3 illustrates the L3 albedo sample, together with inter-comparison implications between NOAA-20 VIIRS albedo and S-NPP VIIRS albedo. The routine validation results with ground measurements are illustrated in Section 4. Finally, cross-comparison with MODIS daily mean albedo is provided in Section 5. A brief summary is presented in Section 6.

## 2. Background and algorithm

### 2.1. Multi-spectral observations from VIIRS onboard S-NPP and NOAA-20

The VIIRS is one of the primary earth-observing instruments (Schueler et al., 2002) onboard the Suomi National Polar-orbiting Partnership (S-NPP, launched on October 28, 2011) and the Joint Polar Satellite System (JPSS) series satellites with daily global coverage. The first JPSS satellite was launched on November 18, 2017, and was renamed as NOAA-20 thereafter (Uprety et al., 2018). One superiority in providing a shortwave albedo product is that the VIIRS presents multi-channel observations over optical spectrum (0.4–12 μm) with advanced technology from the advanced very high resolution radiometer, MODIS, and Defense Meteorological Satellite Program Operational Linescan System (Cao et al., 2018). Shortwave broadband albedo is derived using the VIIRS moderate bands M1–M5, M7–M8, and M10–M11. Band M6 often becomes saturated over snow or desert, whereas band M9 is located in a region with stronger water vapor absorption and more sensitive for thin cirrus detections, which are not used for albedo estimation (Liang et al., 2005b; Cao et al., 2013). For snow-free land LUT regression, M2 and M3 are excluded because of their strong correlation with M1 (Wu et al., 2017). The normalized spectral response functions of certain S-NPP VIIRS and NOAA-20 VIIRS bands were compared to those of Terra MODIS in Fig. 1. Considering the spectral response function (SRF) differences between S-NPP VIIRS and

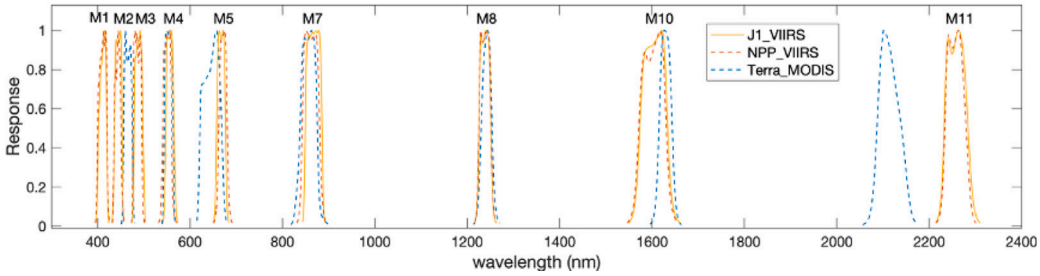


**Fig. 1.** Spectral response function (SRF) of S-NPP/NOAA-20 VIIRS compared with Terra MODIS as reference.

NOAA-20 VIIRS, specific LUTs are prepared for the albedo product production from each sensor. The spectral responses of VIIRS and MODIS show close center wavelengths. Thus, their corresponding shortwave albedo should be comparable, but with a slightly different spectral range and shape.

### 2.2. Level-2 direct estimation method of daily mean blue-sky albedo

The VIIRS daily albedo, referred to as daily mean broadband blue-sky surface albedo, is the ratio between integrals of instantaneous upwelling shortwave radiation $S\uparrow(t)$ and incident shortwave radiation $S\downarrow(t)$ (Wang et al., 2017), where $t$ is the daytime with incident shortwave radiation larger than zero. The instantaneous albedo is represented by Formula (1) and the daily mean albedo is represented by Formula (2).

$$\alpha = \frac{S\uparrow(t)\,dt}{S\downarrow(t)\,dt} \tag{1}$$

$$\overline{\alpha} = \frac{\int S\uparrow(t)\,dt}{\int S\downarrow(t)\,dt} \tag{2}$$

The VIIRS L2 Direct Estimation Method derives surface daily mean albedo from TOA reflectance if no cloud is detected, so the level-1 (L1) TOA reflectance is the main input for the VIIRS albedo estimation. The relationship between TOA reflectance and surface albedo is predictable and approximately linear under specific solar/view geometry on the premise of distinguishing generic and bright surface (Liang et al., 2005a; Wang et al., 2013). The relationship coefficients are stored in LUTs with solar/view geometry, i.e., the solar zenith angle (SZA), view zenith angle (VZA), and relative azimuth angle, declination angle, and latitude as look-up entries. The insolation variation within a day alters the diurnal albedo variation and becomes an important driving factor of daily mean albedo in L2 algorithm (Wang et al., 2015). The incident radiation and its partition between direct and diffuse components are dominated by the solar zenith angle (SZA) and the aerosol under clear-sky conditions. Thus, another two entries, the declination angle ($dec$) of the earth and local time calculated from the latitude ($lat$), are added to predict the diurnal trajectory of SZA in different seasons. Various types of aerosol, including urban, rural, desert, and biomass burning have been considered in the simulation of the TOA reflectance using radiative transfer software (the second simulation of a satellite signal in the solar spectrum, 6S) (Wang et al., 2017).

In addition to a generic LUT trained with data for all surface and aerosol types, specific LUTs are designed for bright surfaces, including snow, bare soil, and sea-ice, as their albedo diurnal variation and magnitude differ significantly when compared against vegetation. Error analysis suggested that separate LUT and accurate surface-type information could improve the estimation accuracy (Qu et al., 2013; Wang et al., 2017). LUT selection is based on surface cover information obtained from the upstream EDRs in order of ice concentration, snow cover, and surface type. Specifically, the sea-ice-specific LUT is selected if the ice concentration value in the sea-ice EDR indicates the presence of sea-ice. For any ice-free land pixel, its binary snow mask is verified to determine whether the snow-specific LUT can be applied. If the pixel is snow-free, but the surface-type data suggest the pixel as bare soil, then the bare-soil-specific LUT is utilized. A generic LUT is used for all other land pixels.

For each index entry $(\theta_s, \theta_v, \varphi_s, lat, dec)$, shortwave daily mean albedo can be estimated by Formula (3)

$$\alpha = c_0(\theta_s, \theta_v, \varphi_s, lat, dec) + \Sigma_b c_i(\theta_s, \theta_v, \varphi_s, lat, dec)\rho_i \tag{3}$$

where $\alpha$ is daily mean broadband blue-sky albedo, containing the dependence of daily albedo on the daily changes in solar illumination; $\theta_s$ is the SZA at the satellite pass time; $\theta_v$ is the view zenith angle (VZA); and $\varphi_s$ is the relative azimuth angle (RAA). Further, $i$ marks the VIIRS moderate resolution channel number, $\rho_i$ is the L1 TOA reflectance from SDRs, and $c_0$ and $c_i$ are the retrieval coefficients, where $c_0$ is the constant term. The coefficients are stored in evenly spaced indexed bins. The LUTs cover SZA from 0° to 80° and VZA from 0° to 80°; here, generic, bare soil and snow LUTs have an angle increment of 5°, while the sea-ice LUT has an increment of 2° (Peng et al., 2018). All LUTs contain RAA from 0° to 180° with an increment of 5°. Latitude indexes span from 90° S to 90° $N$ with a grid size of 10°. The declination angle spans from −23.5° to 23.5° with an increment of 5.875°. The algorithm calculates the coefficients for an actual indexing variable combination through linear interpolation in the surrounding index bin.

Two common concerns would arise to the daily mean albedo values derived from single clear-sky TOA observation. One is the influence from the aerosol change within a day could not be depicted by one single satellite observation; the other is the infeasibility of direct albedo retrieving under cloudy conditions. For the first issue, the algorithm makes an assumption that the atmospheric conditions (aerosol loadings) of the satellite overpass time can represent their daily values. Considering the aerosol loadings will hardly stay constant during a day, this assumption could be regarded as a source of uncertainty in the direct algorithm for daily mean albedo. The second issue is the Direct Estimation Method only applies to clear-sky observations, resulting in gaps in online generated albedo due to cloud contamination. Our mitigation is doing gap filling over cloudy pixels using historical albedo in L2 granular albedo, referred to as the enterprise VIIRS albedo product. Historical albedo established two days prior to the current day is used, which is computed offline based on granule albedo of the preceding days (including the previous 8-day retrievals, plus the current day) and static climatology based on the maximum likelihood estimation (Liu et al., 2013a; Wang et al., 2017). Albedo climatology serves as a critical static input to provide statistics about inter-annual trends and variation of albedo for weight calculation and backup value estimation (Jia et al., 2022).

Future information update about the VIIRS albedo datasets will be released from the NOAA JPSS VIIRS Surface Albedo Project website (Yu et al., 2019b), including links to the data archiving system and Algorithm Theoretical Basis Documents (ATBD) (Liang et al., 2018; Yu et al., 2019a). The monitoring and real-time validation results are also demonstrated on the website (Peng et al., 2019a,b).

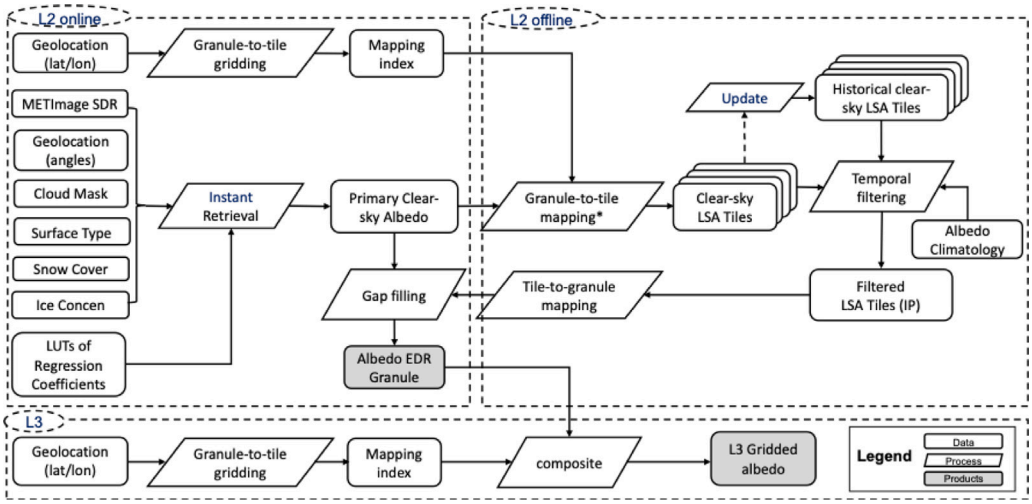


**Fig. 2.** Processing line of VIIRS albedo products including the L2 granule EDR and L3 global gridded albedo. The L2 process includes two components: L2 online and L2 offline; The L3 process is conducted after the end of the whole day's L2 process. Each component is wrapped in dotted boxes separately.

### 2.3. Level-3 global gridded albedo algorithms

Two major procedures are used in the gridded albedo production: a mapping algorithm for the location of granule pixel to grid cell and a composition algorithm for aggregating and compositing multiple pixel albedos to daily grid cell albedo.

The aim is to generate a global albedo map in grids with known earth-based coordinates that can be navigated. Although the granules have been geolocated from geometric distortions, the overlapped pixels in different granules may have varying center latitudes and longitudes and should be projected to a predefined grid system, described as a gridding process (Wolfe et al., 1998). Here, the algorithm separates the gridding function as a mapping tool, shared in the NOAA JPSS land production process.

The global grid, set in Sinusoidal projection at 1-km spatial resolution that maintains an equal area despite conformal distortion, is evenly divided into 72 (horizontal) by 72 (vertical) non-overlapping tiles (NOAA and NASA, 2015). All granule observations for the day are mapped into tile grids. However, many issues may influence the mapping efficiency and accuracy (e.g., larger distortion ratio in polar regions and mapping "holes" when the pixel size is larger than the grid cell, such as at the edge of the scan). To address these issues, the gridding tool adopts the nearest neighbor strategy and forward mapping method (Khlopenkov and Trishchenko, 2008) in a rolling window to generate gap-free correspondence between the granule pixel and grid cell. This includes the list of intersected granules within each tile and the mapping index from granules to tiles. The mapping index is regarded as the pointers of the pixel location in the output grid for each overlapped granule pixel. Meanwhile, the index information guides the reprojection of albedo from granules to tiles.

The composition algorithm uses several criteria to select the "best" albedo value for each grid cell, from the multiple co-located albedo retrievals in L2 granule albedo product. Granules have overlapped areas between neighboring orbits, especially over the high-latitude areas. The overlapped observations have similar fields of view owing to the design features of the VIIRS: controlling the pixel growth rate at the edge of the scan minimizes the bow-tie effect (Cao et al., 2013; Hillger et al., 2013). Meanwhile, the spatial resolution of VIIRS granular albedo (750 m at nadir) is close to the grid cell resolution (1 km). Thus, we assume that the albedo value in granule albedo product can be directly adopted by the co-located grid cell in gridded albedo product through a forward mapping method and nearest sampling strategy.

Data screenings are based on three key factors: retrieval paths (refer to "LUT type"), cloud conditions, and geometry angles, which are considered through a hierarchy of criteria. With the same cloud condition and L2 data validity, retrievals with favorable SZAs/VZAs (<60°) are classified as high-quality candidates. Meanwhile, the other clear-sky retrievals are assigned to the mid-quality group, considering their increased uncertainty at larger SZAs or VZAs Wang et al. (2017), Liu et al. (2009a) and Román et al. (2010). The cloudy-sky values are placed in the low-quality group. Within each group, albedo retrievals may be derived from different LUTs (e.g., snow, sea-ice, and others). Among them, the snow value is preferably than sea-ice and then others. For instance, a grid cell has overlap with three pixels with high-quality albedos. Out of the three pixels, one pixel is a snow pixel. Thus, the albedo of this single pixel is used as L3 albedo, although there are more pixels with high-quality albedos in the grid cell. Snow and ice albedos are preserved to the extent possible considering their strong influence on climate, surface energy balance, and large-scale modeling (Gleeson et al., 2014; Kumar et al., 2020; Gardner and Sharp, 2010; Fletcher et al., 2015; Wang et al., 2016a). Finally, the median albedo value of the prioritized LUT category within the highest priority group is assigned as L3 albedo in the grid cell. Accordingly, the screening combinations are set as quality flags for each grid cell, including the overall quality, cloud condition, and retrieval path. The composited albedo tiles over the globe make up a global map on the Earth grid. "High quality" indicates that the albedo is derived from direct retrieval with a favorable SZA and VZA; "median-quality" retrievals are from Direct Estimation Method, but with large zenith angles; and "low-quality" values are from offline gap-filling using temporally filtered albedo from 2 days ago. The cloud mask and retrieval path flags are inherited from the selected L2 retrievals.

Fig. 2 shows the data flow of the enterprise VIIRS albedo algorithm, including the L2 granular albedo processing and the L3 gridded albedo production. Following the data blocks, we can determine the required input data in the albedo estimation and how they are converted to the final daily gridded albedo step-by-step. The clear-sky daily mean albedo estimation is completed in the L2 online process, and granular albedo would be gap-filled in the L2 offline process. The result is then fed to the L3 process to generate gap-free daily gridded albedo.

### 2.4. In-situ daily mean albedo estimation and scale difference assessment from high-resolution albedo

Representative ground-based surface shortwave albedo, calculated from the upward and downward radiation measured by pyranometers mounted on towers, have been used to assess the absolute accuracy of satellite albedo products (Zhou et al., 2016; Liu et al., 2009a; Jin

**Table 1**
Stations used in the validation.

| ID | Network | Sitename | Lat [°] | Lon [°] | Ele [m] | Surface type |
|---|---|---|---|---|---|---|
| 1 | SURFRAD | Bondville_IL | 40.050 | −88.370 | 230 | Crop |
| 2 | SURFRAD | Boulder_CO | 40.125 | −105.237 | 1689 | Grassland |
| 3 | SURFRAD | Desert_Rock_NV | 36.624 | −116.019 | 1007 | Shrub |
| 4 | SURFRAD | Fort_Peck_MT | 48.310 | −105.100 | 634 | Grassland |
| 5 | SURFRAD | Goodwin_Creek_MS | 34.250 | −89.870 | 98 | Pasture |
| 6 | SURFRAD | Penn_State_PA | 40.720 | −77.930 | 376 | Crop |
| 7 | SURFRAD | Sioux_Falls_SD | 43.730 | −96.620 | 473 | Crop |
| 8 | ARM | sgpsirsC1 | 36.605 | 97.485 | 318 | Grassland |
| 9 | ARM | sgpsirsE9 | 37.133 | 97.266 | 386 | Pasture |
| 10 | ARM | sgpsirsE11 | 36.881 | 98.285 | 360 | Pasture |
| 11 | ARM | sgpsirsE12 | 36.841 | 96.427 | 331 | Prairie |
| 12 | ARM | sgpsirsE13 | 36.605 | 97.485 | 318 | Pasture |
| 13 | ARM | sgpsirsE15 | 36.431 | 98.284 | 418 | Pasture |
| 14 | ARM | sgpsirsE31 | 37.151 | 98.362 | 412.1 | Pasture |
| 15 | ARM | sgpsirsE32 | 36.819 | 97.820 | 328 | Pasture |
| 16 | ARM | sgpsirsE33 | 36.926 | 97.082 | 357 | Grassland |
| 17 | ARM | sgpsirsE34 | 37.069 | 96.761 | 417 | Pasture |
| 18 | ARM | sgpsirsE35 | 35.862 | 97.070 | 294.1 | Pasture |
| 19 | ARM | sgpsirsE36 | 36.117 | 97.511 | 336.8 | Pasture |
| 20 | ARM | sgpsirsE37 | 36.311 | 97.928 | 378.9 | Grassland |
| 21 | ARM | sgpsirsE38 | 35.880 | 98.173 | 371.2 | Pasture |
| 22 | ARM | sgpsirsE39 | 36.374 | 97.069 | 279 | Pasture |
| 23 | ARM | sgpsirsE40 | 36.319 | 96.762 | 247 | Pasture |
| 24 | ARM | sgpsirsE41 | 36.880 | 97.086 | 340 | Grassland |
| 25 | BSRN | Budapest | 47.429 | 19.182 | 139.1 | Grassland |
| 26 | BSRN | Cabauw | 51.971 | 4.927 | 0 | Grassland |
| 27 | BSRN | Gobabeb | −23.561 | 15.042 | 407 | Desert |
| 28 | BSRN | Georg_von | −70.650 | −8.250 | 42 | Ice |
| 29 | BSRN | Izana | 28.309 | −16.499 | 2372.9 | Mountain top |
| 30 | BSRN | Payerne | 46.815 | 6.944 | 491 | Crop |
| 31 | BSRN | Selegua | 15.784 | −91.990 | 602 | Grassland |
| 32 | BSRN | Tateno | 36.058 | 140.126 | 25 | Grassland |
| 33 | BSRN | Toravere | 58.254 | 26.462 | 70 | Grassland |
| 34 | NEON | Abby_Road | 45.762 | −122.330 | 365 | Evergreen forest |
| 35 | NEON | Bartlett | 44.064 | −71.287 | 274 | Deciduous forest |
| 36 | NEON | Blandy | 39.034 | −78.042 | 183 | Deciduous forest |
| 37 | NEON | Central_Plains | 40.816 | −104.746 | 1654 | Grassland |
| 38 | NEON | Dakota_Coteau | 47.162 | −99.107 | 575 | Grassland |
| 39 | NEON | Dead_Lake | 32.542 | −87.804 | 25 | Evergreen forest |
| 40 | NEON | Disney_Wild | 28.125 | −81.436 | 20 | Pasture |
| 41 | NEON | Great_Smoky | 35.689 | −83.502 | 575 | Deciduous forest |
| 42 | NEON | Guanica_Forest | 17.970 | −66.869 | 125 | Evergreen forest |
| 43 | NEON | Harvard_Forest | 42.537 | −72.173 | 348 | Deciduous forest |
| 44 | NEON | Healy | 63.876 | −149.213 | 677 | Shrub |
| 45 | NEON | Jones | 31.195 | −84.469 | 47 | Crop |
| 46 | NEON | Jornada_LTER | 32.591 | −106.843 | 1324 | Shrub |
| 47 | NEON | Klemme_Range | 35.411 | −99.059 | 519 | Grassland |
| 48 | NEON | Konza_Prairie | 39.101 | −96.563 | 324 | Deciduous forest |
| 49 | NEON | Lajas | 18.021 | −67.077 | 16 | Crop |
| 50 | NEON | LBJ_National | 33.401 | −97.570 | 272 | Deciduous forest |
| 51 | NEON | Lenoir_Landing | 31.854 | −88.161 | 13 | Deciduous forest |
| 52 | NEON | Lower_Teakettle | 37.006 | −119.006 | 2149 | Evergreen forest |
| 53 | NEON | Mountain_Lake | 37.378 | −80.525 | 1170 | Deciduous forest |
| 54 | NEON | Moab | 38.248 | −109.388 | 1799 | Evergreen forest |
| 55 | NEON | Northern_GP | 46.770 | −100.915 | 589 | Grassland |
| 56 | NEON | North_Sterling | 40.462 | −103.029 | 1350 | Crop |
| 57 | NEON | Oak_Ridge | 35.964 | −84.283 | 344 | Deciduous forest |
| 58 | NEON | Ordway_Swisher | 29.689 | −81.993 | 46 | Wetland |
| 59 | NEON | Smithsonian | 38.893 | −78.139 | 352 | Deciduous forest |
| 60 | NEON | Smithsonian_E | 38.890 | −76.560 | 33 | Crop |
| 61 | NEON | San_Joaquin | 37.109 | −119.732 | 400 | Evergreen forest |
| 62 | NEON | Soaproot_Saddle | 37.033 | −119.262 | 1210 | Evergreen forest |
| 63 | NEON | Santa_Rita | 31.911 | −110.835 | 997 | Shrub |
| 64 | NEON | Steigerwaldt | 45.509 | −89.586 | 476 | Deciduous forest |
| 65 | NEON | Talladega | 32.950 | −87.393 | 166 | Deciduous forest |
| 66 | NEON | Treehaven | 45.494 | −89.586 | 467 | Deciduous forest |
| 67 | NEON | Uni_Kansas | 39.040 | −95.192 | 322 | Deciduous forest |
| 68 | NEON | UNDERC | 46.234 | −89.537 | 521 | Deciduous forest |
| 69 | NEON | Utqia | 71.282 | −156.619 | 4 | Wetland |
| 70 | NEON | Woodworth | 47.128 | −99.241 | 591 | Wetland |
| 71 | NEON | Wind_River | 45.820 | −121.952 | 351 | Evergreen forest |

et al., 2003; Wang et al., 2018a; Li et al., 2018; Song et al., 2019). Four radiation networks, namely, surface radiation budget network (SURFRAD) (Driemel et al., 2018a; Augustine et al., 2005), atmospheric radiation measurement (ARM) (Liu et al., 2009b; Stokes and Schwartz, 1994), baseline surface radiation network (BSRN) (Driemel et al., 2018b), and national ecological observatory network (NEON) (Metzger

et al., 2019), are deployed in our long-term monitoring (LTM) to represent the various land covers and topography conditions. The seven sites of SURFRAD cover a variety of vegetation climate types in the United States and are well-maintained. The 17 sites in ARM are mainly distributed in the Southern Great Plains (SGP) atmospheric observatory, and they possess almost exactly the same configuration and radiation measurement equipment as those in the SURFRAD sites. Both the SURFRAD and SGP release data on daily basis, so the validation result could be updated on a weekly basis in our validation system. The BSRN is a baseline network for surface radiation and composed of worldwide sites. The NEON terrestrial tower sites are located across 20 eco-climatic domains in the United States with various vegetation types and climates.

All 71 sites contain appropriate tower sites with the necessary infrastructure, such as human maintenance and data preprocessing, to measure radiation variables for albedo calculations. The site details are listed in Table 1. The preferred value of the downwelling solar flux is obtained from the diffuse solar irradiance and direct-normal irradiance multiplied by the cosine of the solar zenith angle to reduce the infrared cooling problem. When the direct-normal and diffuse solar radiation measurements are unavailable, the global solar measurement is used (Wang et al., 2012a).

The daily mean blue-sky albedo from the tower measurements involves the upward and downward shortwave flux in the entirety of the daytime. The observed fluxes and thus the albedo are impacted by the presence of clouds. Hereinafter, the comparison retains only the clear-sky conditions to exclude the uncertainty from cloud effect (Wu et al., 2017; Stroeve et al., 2013; Roman et al., 2013). The cloudy measurements were screened before calculating daily mean albedo. The cloud flag was derived from ground measured down-welling radiation referring to the method of (Stroeve et al., 2001), assuming the incoming solar radiation is lower under cloudy conditions than clear-sky situations during the same season. The method shows promising results, so we adopted the following criterion: if the ratio of the measured incoming solar radiation to that simulated is larger than 0.8, a clear sky condition is assumed. In our practice, the simulated clear-sky downwelling radiation is expressed as a function of the Linke turbidity factor (TL, for an air mass equal to 2) through a compact and convenient radiation transfer model (Remund et al., 2003; Wald, 2018). The TL value would be initialized and then optimized in iteration with the recognized cloudy observations being removed each round until convergence has been reached.

A data quality flag ($DQF$) for the in-situ daily mean albedo is provided on a daily basis. This indicates the clear-sky measurements availability during daytime, limited by local times between 5 am and 8 pm with positive downward and upward radiation. Only with sufficient clear-sky observations is the $DQF$ set as high (encoded as 0). Here, we set a count threshold of 360 for minute-interval measurements (equivalent to 6 h worth of sample number). Otherwise, clear-sky blue-sky albedo during local 9~10 am or 2~3 pm is used as the alternative with a $DQF$ of 1, as the albedo diurnal variation suggested these two periods mostly contain the intersection with the daily mean blue-sky-albedo line (Wang et al., 2015). For other cases, in-situ albedos are regarded as cloudy, and $DQF$ is stored as 2. Only the matchups with $DQF$ of 0 or 1 are included in the site-specific validation to guarantee the reliability of the reference data. All the validation results have been updated weekly to monitor the albedo performance since the enterprise VIIRS albedo became operational in Sep 2019. Here, we used the matchups until Apr 2022 for analysis.

A primary challenge in albedo validation based on ground measurements is the inadequate spatial representativeness of in-situ observations in some sites because of the surface heterogeneity, as revealed by the previous studies (Liu et al., 2009a; Moustafa et al., 2017; Wang et al., 2012b; Wu et al., 2014; Wang et al., 2014, 2016b). The heterogeneity condition varies according to the land cover change in different seasons. A higher resolution albedo product at 30-m resolution is used to simulate the surface variability near each of the site. Its influence on albedo is characterized by two indices, the scale difference and the sub-pixel variability. The former is the observed difference between area-based satellite retrieval and point-based station measurement. It is a clear and specific value, which is similar to the validation bias. However, this is based on an accurate depiction of the satellite pixel boundary, which could be accurately described for geostationary sensors such as GOESR ABI with a fixed view location and view angle. However, this could only be approximately characterized for polar satellite sensors like VIIRS with a constantly changing footprint of view (FOV). The latter is defined as the within-pixel standard deviation (std), which demonstrates the variation degree of the sub-pixel albedo within the satellite FOV. For VIIRS pixel, although the view angle and projection center varies, a larger std indicates potentially higher impact from the site surrounding albedo variation to the validation error.

Specifically, the scale difference is calculated as the Landsat albedo difference between the area "seen by" the ground instrument and a larger area "seen by" the co-located VIIRS pixel. Both albedo values are aggregated as the mean of Landsat albedo by projecting the VIIRS pixel and ground instrument footprint to the Landsat albedo images. Here, the VIIRS pixel's FOV is approximated as a 1-km diameter circle. The tower observation's FOV is depicted as a circle with a radius determined by the mounting height of radiometer (Franch et al., 2014), i.e., the instrument's FOV at SURFRAD sites is represented by a circle with a diameter of 70 meters which accounts for 90% of the cosine response.

Landsat 8 albedo is approximated using a broadband reflectance value, which has been derived based on an NTB conversion method (Wang et al., 2016b) without anisotropy correction. This exists in both aggregated albedo values, and it should not have a significant impact on the albedo scale difference pattern after the deviation calculation. More importantly, the cloud/cloud shadow masks and the snow flag in the Landsat −8 surface reflectance product quality (Zhu et al., 2015) was carefully reviewed to remove the cloudy pixels and distinguish the snow covered and snow-free periods. The selected samples are all clear within the VIIRS pixel area to exclude cloud contamination. Considering that the clear-sky Landsat images during the study period cannot sufficiently reveal the seasonal feature of the albedo scale difference, we have extended the period of Landsat 8 data back to 2014.

### 2.5. Inter-comparison and cross-comparison

The VIIRS sensors onboard NOAA-20 and S-NPP share the same orbit but are separated in time by approximately 50 min. The enterprise algorithm runs simultaneously on data from the two satellites, while each can generate a daily global albedo map. The two products are expected to be consistent with each other, with a slight difference due to changing atmospheric conditions, surface dynamics and difference in satellite viewing angles. The inter-comparison between S-NPP and NOAA-20 VIIRS albedo evaluates the impact of these factors on the albedo product. Regarding bright surfaces, such as bare soil and snow surfaces, the comparison residual has shown some features related to strong forward scattering, which can be demonstrated as a dependence on the scattering angle, $\xi$, that is, the angle between the illumination (sun) and observation (satellite), as shown in Formula (4).

$$cos(\xi) = cos(\theta_s)cos(\theta_v) + cos(\phi_s - \phi_v)sin(\theta_s)sin(\theta_v) \quad (4)$$

The NOAA-20 and S-NPP albedo difference has been evaluated in spatial and temporal dimensions, and among various LUT types.

Cross-comparison with other global albedo products, such as MODIS, is also indispensable because ground measurements can only represent limited surface cover and climate types. However, the challenge is that, for an "apple-to-apple" comparison, the daily mean blue-sky albedo should be used to simulate the BRDF products as reference rather than the supplied instantaneous albedo. The daily mean albedo is the ratio between the daily upward and downward

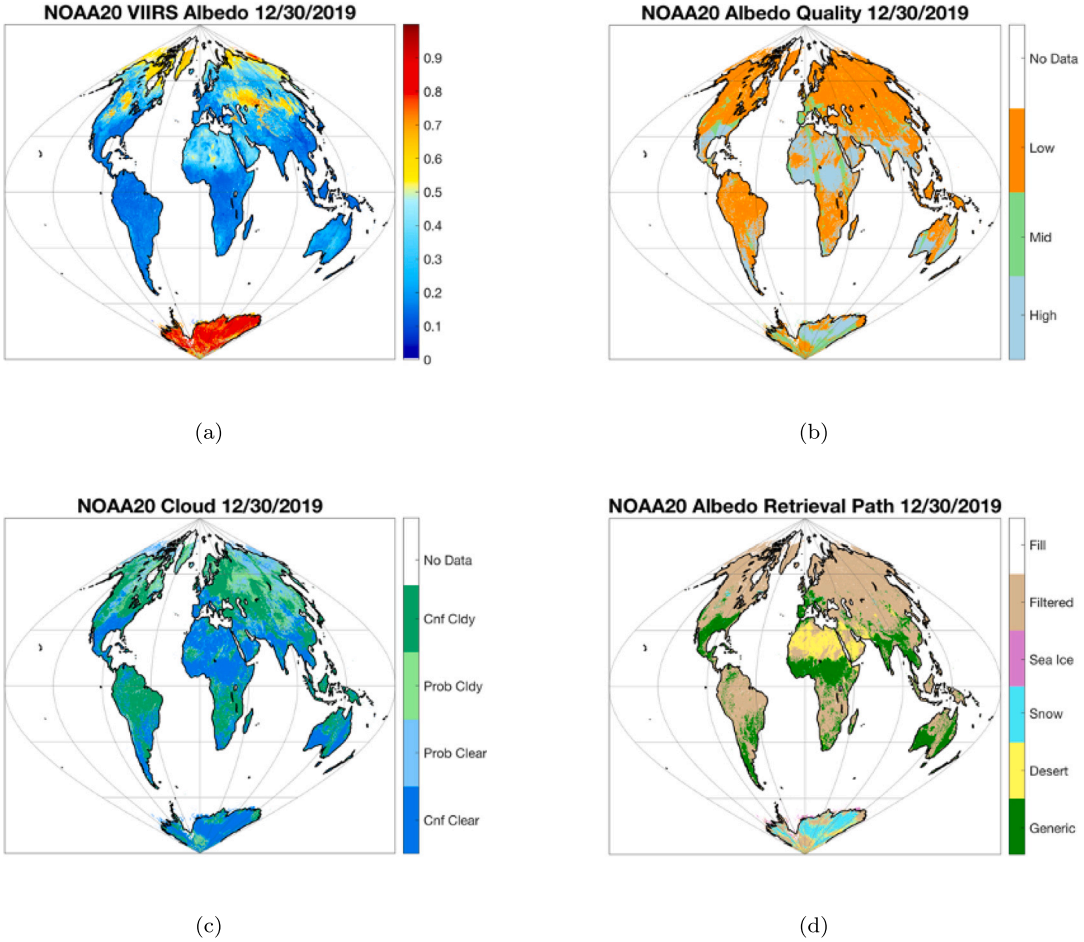


**Fig. 3.** Daily composite of NOAA-20 VIIRS surface albedo acquired Dec 30, 2019. Datasets: NOAA-20 daily gridded global albedo (a), overall quality (b), cloud mask flag (c), and retrieval path flag (d).

shortwave fluxes, where the daily upward energy is derived by integrating the product of instantaneous albedo and downward flux through the daytime (Wang et al., 2015; Potter et al., 2020). As a fundamental basis, the BRDF is a mathematical tool to describe the surface anisotropy, with incidence and reflected directions as parameters. Angular integration based on BRDF function provides the black-sky albedo (BSA) at a specific SZA and the white-sky albedo (WSA) (Schaaf et al., 2002), which can further be combined into the instantaneous blue-sky albedo with the skylight ratio as a regulating factor (Román et al., 2010).

MODIS BRDF parameters are supplied at a spatial resolution of 500 m (MCD43A1), with the quality information (MCD43A2) being utilized to screen the high-quality pixels (full inversion with adequate input samples) as the producers recommended (Wang et al., 2016b). MODIS high-quality full inversion products are only recommended for use up to a 70° SZA, as the anisotropic model often has difficulties at SZAs higher than this threshold. MOD08 provides the AOD to index the diffuse skylight factor from a pre-stored LUT derived from MODTRAN5 simulations. Note that the multiple scattering between surface and atmosphere was not considered here, which is acceptable for snow-free surface and will introduce slight uncertainty for a snow surface (Wang et al., 2014). To sum up, we use the comparison results with MODIS pixels with full retrieval with clear sky observations over the day of interest and without extremely large SZAs for the final statistics.

The snow cover is an essential input for albedo algorithms in determining the retrieval path, so the upstream snow cover quality has a significant influence on the albedo accuracy. Since we have observed some albedo difference due to the snow mask difference, we have introduced another independent snow cover product (the interactive multi-sensor snow and ice mapping system, IMS) as reference to understand the snow albedo difference between MODIS and VIIRS. The IMS snow cover dataset is generated by NOAA and has been widely used (Ramsay, 1998; Helfrich et al., 2007). Its reliability comes from the combination of observations from geostationary and polar orbiting satellites in the visible, infrared, and microwave spectra, as well as manual analyst input (Chiu et al., 2020).

## 3. VIIRS composited albedo and inter-comparison

### 3.1. Daily composites

An example of the NOAA-20 global gridded albedo product is shown in Fig. 3, graphing the albedo and its quality variables.

In this case, albedo has complete coverage, except for northern Greenland, which is characterized by the absence of solar radiation during polar night. Complete global coverage represents the common operational status unless there are any sporadic data missing from L1b level. The albedo map shows continuous albedo distribution over all-sky conditions, indicating the consistency between different retrieval paths. Moreover, the composition process suppresses the random noise in direct retrievals when multiple observations overlay, as the median value within the highest-quality group is used as the final value. The choice of the median value, rather than the mean value, is because it is less affected by outliers and skewed data. Fig. 4 provides a daily tile count map, that is, the count of overlaid L2 observations after mapping to the grid. For 1- and 2-layer cases, the majority over low and median latitude regions and the mean and median calculations

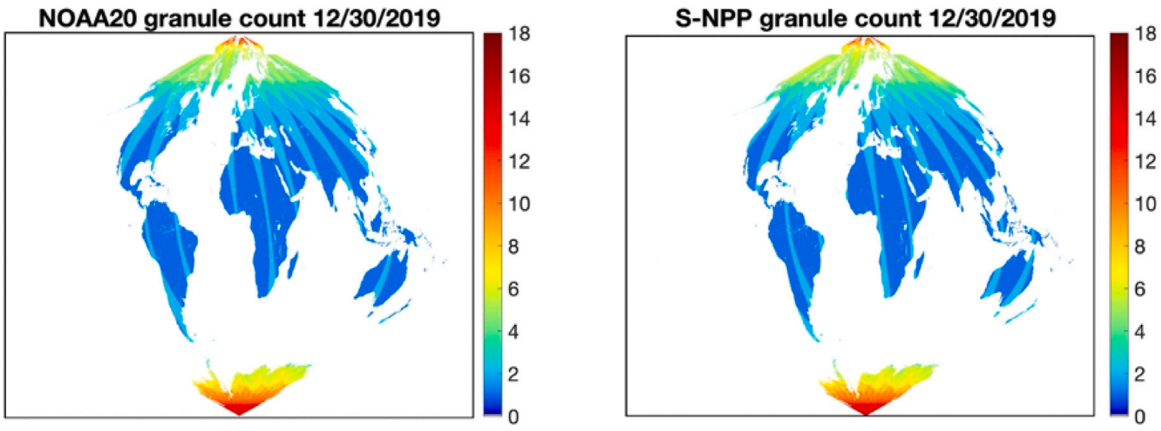


**Fig. 4.** Number of overlapping image tiles obtained from the L2 granule albedo product of NOAA-20 (left) and S-NPP (right) on Dec 30, 2020.

are identical. For more-than-two-layer cases, the median method could generate result with less outliers. Further, the use of the median value can maintain the original albedo value and its corresponding quality flag, which benefits the uncertainty assessment of the algorithm.

We counted the clear-sky daily retrievals in a year using the cloud information in the L3 albedo quality flag to identify the areas with more retrievals from the main algorithm (Fig. 5) as clear-sky observation is a pre-requisite for the Direct Estimation Method. The count numbers are based on the cloud condition at the satellite overpass time in each day. We can observe that some areas are associated with frequent clear-sky conditions, such as North Africa, Western United States, and West Australia. In contrast, some areas show a more occurrence of cloudy-sky conditions, such as Northeast South America, Southern west Africa, and Tibetan region.

### *3.2. Comparison between S-NPP and NOAA-20 VIIRS albedo*

#### *3.2.1. Daily composite comparison*

Fig. 6 displays the global composite albedo from NOAA-20 and S-NPP and their difference. This indicates a very similar spatial distribution and magnitude between the two albedos in both the June and December cases. Taking the Dec 30, 2019 as an example 6(f), the mean difference between SNPP and NOAA-20 albedo over generic land surface is −0.002 (<1%); the RMD over bare soil surface is −0.007 (<2%); the RMD over snow is −0.037 (<5%); and the RMD over sea ice is −0.007 (<2%).

We also observe that the difference maps illustrate orbit-related patterns as alternating light blue and red strips (Figs. 6(e) and 6(f)). This reveals the influence from the same-day S-NPP VIIRS and NOAA-20 VIIRS observations in terms of solar and view geometry, as well as instrument calibration. The VZA and SZA play significant roles in the retrieval of surface albedo. The VZA directly influences the pixel "footprint" projected onto the Earth's surface (Gladkova et al., 2016); the larger the VZA, the larger the footprint and the broader the horizontal sampling interval, which may cover heterogeneous land surfaces, affecting the integrity of the retrieved albedo values. In parallel, the SZA impacts the solar insolation conditions under which the albedo is retrieved.

The albedo difference suggests a correlation with the VZA difference as Fig. 7 shows. The albedo difference from the generic land LUT slightly increases with the VZA difference 7(a), which apparently can be separated into two parallel trend lines by the SZA difference (Figs. 7(b) and 7(c)), and the albedo difference has the same sign as the SZA difference. SZA influences the Atmospheric Scattering; a higher SZA increases scattering and potentially affects albedo retrieval. Also The SZA could affect how different land cover types (e.g., forests, grasslands, and deserts) reflect sunlight, impacting the accuracy of the LUT-based albedo retrieval. Besides, The lookup table is generated based on a selected set of BRDF samples and the representativeness and uncertainty at different SZAs vary. Therefore, the difference in albedo reflects the impact of varying observation conditions and the limitations in the LUT, especially in the SZA dimension.

The residual in bare soil direct retrievals demonstrates a different feature (Fig. 8). As a bright surface, the desert BRDF shows nearly isotropic reflectance, but with enhanced reflectance in the forward direction. The samples show different distributions in two groups divided by around 70° of the scattering angle $\xi$. For the pixel cluster with the scattering angle of either NOAA-20 or S-NPP smaller than 70° when backscattering occurs (i.e., when the sensor views the surface with the sun behind the sensor), the albedo difference shows slow linear variation with the VZA difference. Statistically, a larger VZA difference would result in a slightly larger albedo difference. The albedo agrees the best when the VZA difference is zero, as demonstrated in Fig. 8(a). Conversely, when forward scattering dominates with NOAA-20 or S-NPP as both scattering angles are larger than 70° (Fig. 8(b)), the albedo difference demonstrates a negative correlation with the VZA difference. This suggests that the uncertainty in bare soil varies with the scattering angles.

The snow albedo difference also shows a negative correlation with the scattering angle, due to the strong forward scattering characteristics of the snow surface (Fig. 9). Clearly, both the magnitude and scatter of the albedo deviation increase at larger scattering angles, especially when these are larger than 60°. The scattered matchups mainly distribute in the Antarctica region around the edge of a clear-sky area, which is possibly impacted by the undetected cloud coverage. The snow albedo difference between NOAA-20 and S-NPP has a negative bias. This bias would be eliminated after applying the latest NOAA-20 snow LUT in the operational system, which provides a calibration to the NOAA-20 spectral response function and is in the queue to be officially updated.

#### *3.2.2. Time-series comparison between NOAA-20 and S-NPP VIIRS*

Considering the orbit pattern in the difference between NOAA-20 and S-NPP albedo, the global average albedo difference is expected to be reduced if aggregated over a period. This aggregation is a simple average process upon the valid albedo values in a period. Fig. 10 demonstrates the spatial statistics of the global albedo difference after performing temporal aggregation over a period with an increasing day number from 1 to 16. Not only the mean value 10(a) but also the standard deviation 10(b) of the albedo difference between NOAA-20 and S-NPP VIIRS gradually reaches a lower or stable level. The decreasing pattern of the standard deviation is repeatable in different times; however, the mean of error may decrease or retains at a stable level, reflecting the difference between NOAA-20 and S-NPP, mostly less than 0.005, due to the calibration difference in SDR and inconsistency in LUTs.

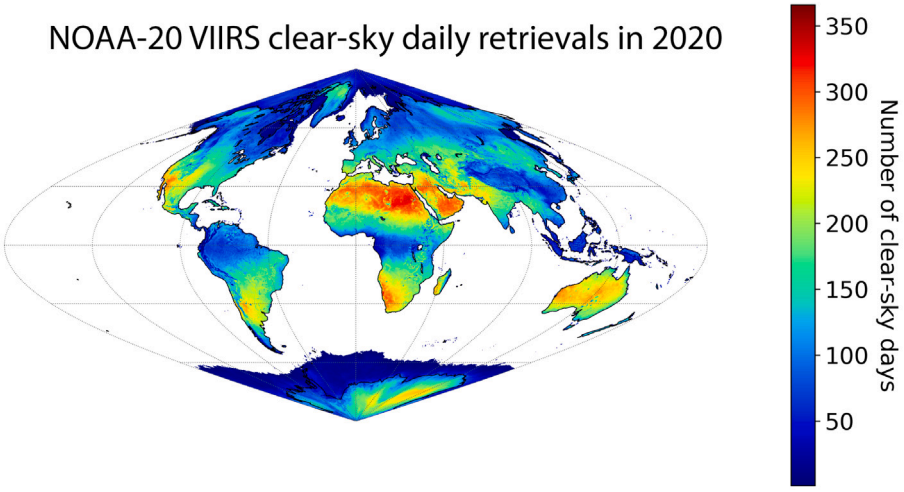


(a)

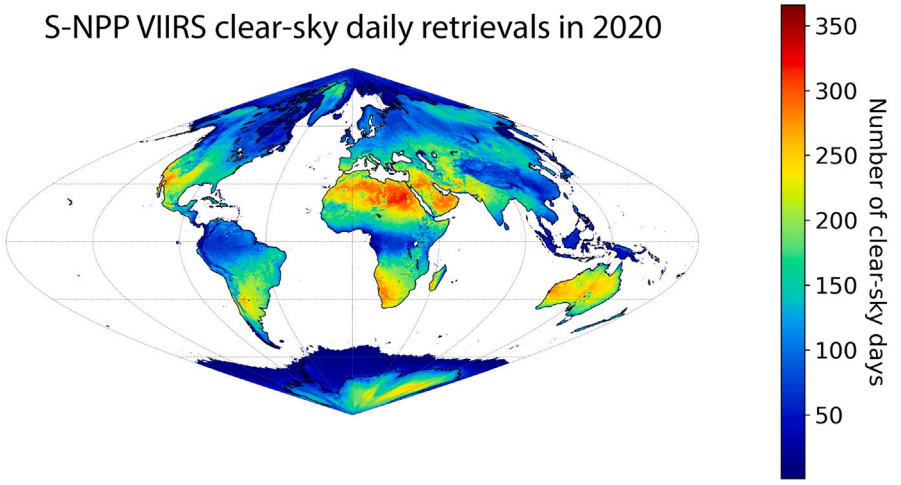


(b)

**Fig. 5.** Global map of number of clear-sky retrievals in L3 VIIRS albedo: (a) NOAA20; (b) S-NPP.

Generally, the spatial mean of global albedo difference in Fig. 11(a) suggests the consistent magnitude of the two albedo products. The mean difference over globe is generally 0.005, while it temporally increases to 0.013 during February. The relative mean difference over global is up to 4%, the relative mean difference over the northern hemisphere is less than 4.1%, and that over the southern hemisphere is less than 2%. The mean of the NOAA-20 and S-NPP albedo difference over the southern hemisphere shows a stronger variation, accompanying the influence from the variation of the sample size and sample distribution. From April to August, the snow and sea ice sample sizes over the Antarctic are relatively low due to the polar night, and the mean albedo difference is relatively small. Meanwhile, the mean albedo difference increases from October to March, along with an increase in snow coverage. For instance, the snow albedo difference over the Antarctic region can be observed in Fig. 6, mainly related to the cloud cover difference, snow cover inconsistency, and snow LUT uncertainty between angles. The snow cover inconsistency (i.e., marked as snow in one product but snow-free in another) would result in the difference of the LUT type used in retrieving albedo between the two sensors. Second, a magnitude difference can be observed between directly retrieved snow albedo and cloudy filled snow albedo retrieval, due to the underestimation of historical albedo using bare soil LUT. This only stands out when observing inconsistent cloud covers at different satellite pass times. Snow cover data change, and an update of albedo climatology with the most recent observations would help address this issue. The snow albedo inconsistency between the results from different angles is orbit-related (Fig. 10). Regarding the north hemisphere, the mean of the NOAA-20 and S-NPP albedo difference remains smaller, but also fluctuates with the sample size and snow season 11(b). It is caused by the similar reason as in south hemisphere, as well as due to season shift.

## 4. Ground measurements validation

Direct validation deploys ground measurements counterpart as an independent reference, and the difference is commonly used to characterize the product accuracy and precision. In this study, VIIRS albedo is compared with the in-situ clear-sky albedo counterpart from the globally distributed sites listed in 1 for evaluation. Fig. 12 presents the overall scatterplots with all high-quality matchups between September 2019 and April 2022 for NOAA-20 and S-NPP, respectively, spanning from September 2019 to April 2022. Overall, both VIIRS albedos show a very small negative bias and a precision of approximately 0.04, compared with the in-situ measurements, which is comparable to similar

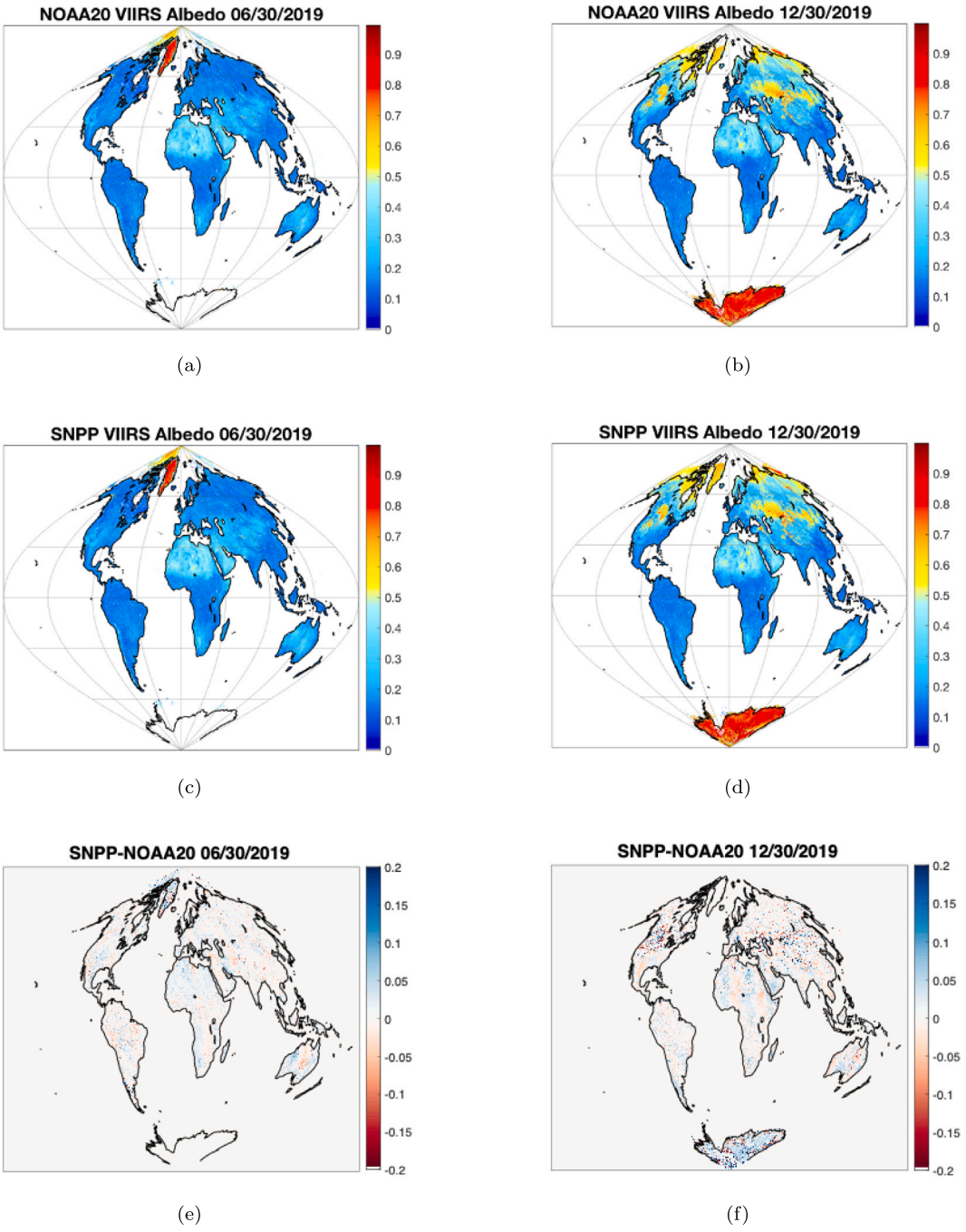


**Fig. 6.** Global albedo composite on June 30, 2019 (left column) and 12/30/2019 (right column). Datasets: (a) and (b) are the NOAA-20 albedo maps; (c) and (d) are the S-NPP albedo maps; while the difference maps between NOAA-20 and S-NPP are demonstrated in (e) and (f).

albedo products (Wang et al., 2018b; Lellouch et al., 2020). The NOAA-20 and S-NPP VIIRS albedo retrievals are quite consistent, which agrees with the conclusion from the global inter-comparison.

Site-specific results are shown in Fig. 13, while the site-specific heterogeneity indices are illustrated in (Fig. 14). The ground sites cover various surface types including crop, grassland, forest, and shrub across different seasons, and they reveal the performance of all three land LUTs (for snow, desert, and generic other). Further, a distinction is made between ground measurements with $DQF$ of 0 (representing high quality with clear sky most of the day, marked with blue label and dots) and 1 (representing degraded quality due to cloudy contamination, marked as red label and dots). High-quality albedo generally outperform the degraded matchups as expected. However, the difference is not significant, and the result of matchups with $DQF$ of 1 shows similar statistics compared to those of all-clear-sky matchups with $DQF$ of 0 in most stations.

Most land pixels, except for snow or bare soil, are retrieved from the generic LUT, including many vegetation types (e.g. grass, crop, forest, and shrub, etc.). The results at most sites demonstrate the reliability of the generic LUT, which is 24% of the sites with a bias within ±0.01, 58% of the sites with a bias within ±0.02, and 75% of the sites have a bias within ±0.03. An extremely good agreement between the two independent albedo estimates is observed at grassland covered sites like sgpsirsE37, sgpsirsE41, Selegua, Dakota_Coteau, et al. at forest covered sites such as Abby_Road, Talladega, Guanica_Forest, et al. for both

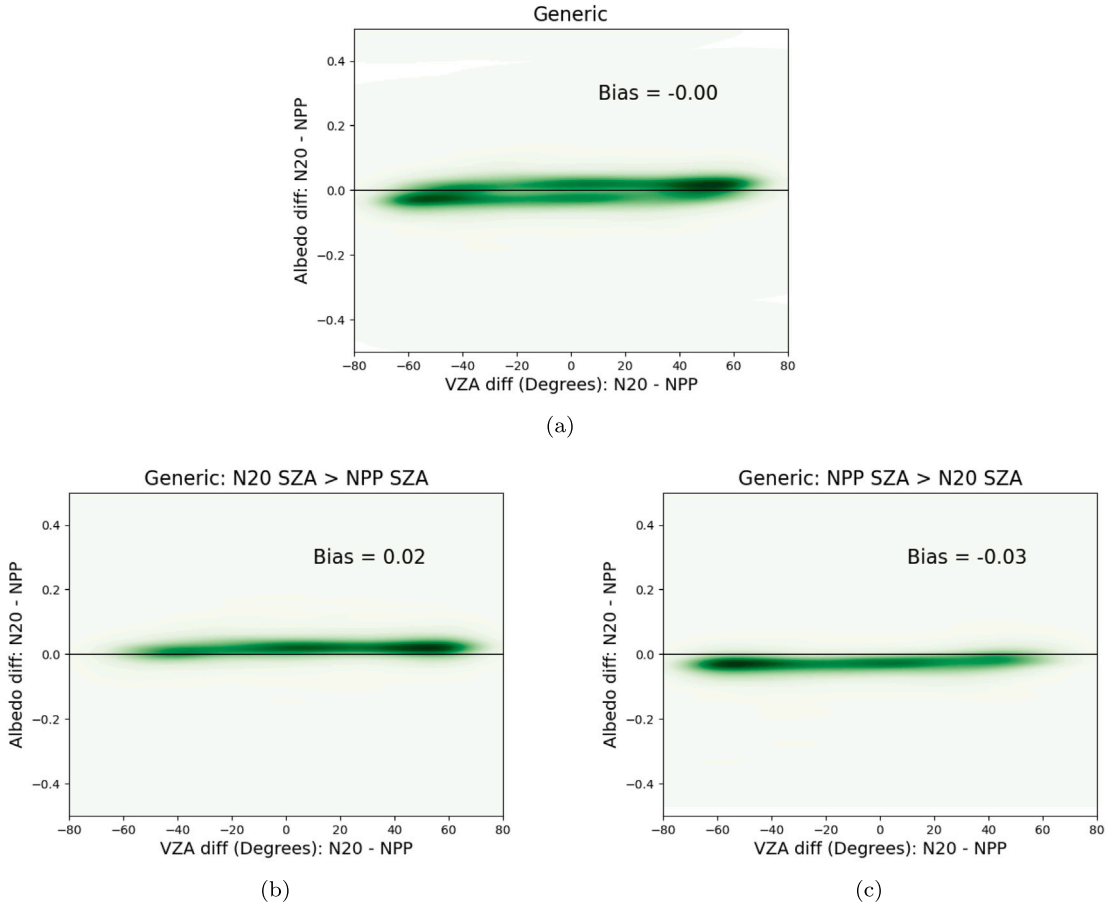


**Fig. 7.** Scatter density plots are used to display the variation in albedo differences relative to the VZA differences between NOAA-20 and S-NPP, based on generic land retrievals. It was observed that the data pairs could be divided into two clusters based on the SZA values: (a) all pixels, (b) when the SZA of S-NPP is smaller than that of NOAA-20, and (c) when the SZA of S-NPP is larger. Areas of higher density are represented in darker color. (Date of data: Dec 30, 2019).

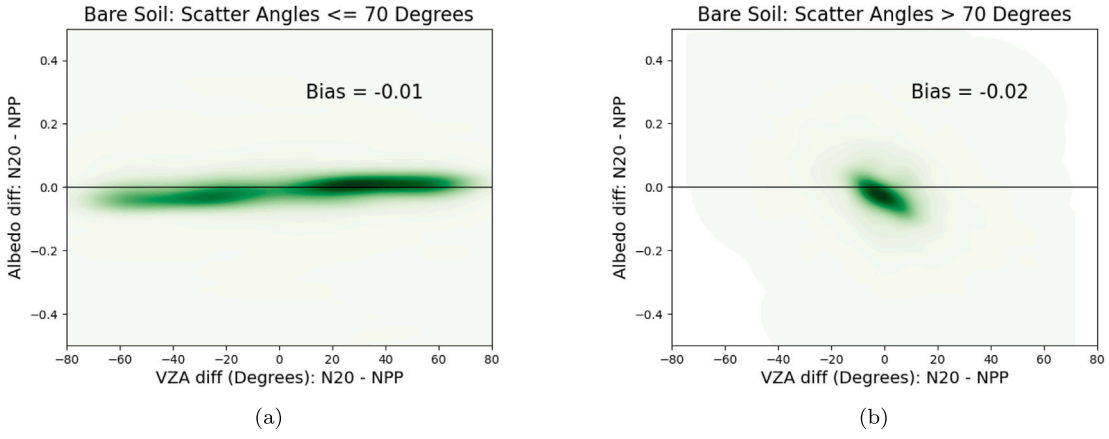


**Fig. 8.** Scatter density plot showing the variation of the albedo difference with the VZA difference between NOAA-20 and S-NPP over bare soil retrievals on Dec 30, 2019. (a) Scattering angles in S-NPP and NOAA-20 are smaller than 70°. (b) When both are larger than 70°. The darker color represents higher density.

snow-free and snow covered albedo. A fairly good consistency is observed between the wetland sites including Ordway_Swisher, Utqia, and Woodworth. One representative crop site is Bondville_IL, whose typical feature is its seasonal heterogeneity pattern due to the mosaic of crop and non-crop patches. It is shown that the satellite albedo is slightly lower than the ground counterpart, which is consistent as the findings in validating the MODIS albedo product (Liu et al., 2009b). When it comes to the shrub surface, represented by the Desert_Rock_NV (DeFries et al., 1995), the VIIRS albedo shows a slight over-estimation and scattered error compared to in-situ albedo. The bias in the difference is due to the albedo scale difference and the scattered variation results from direct estimation noise over the shrub surface. This is similar as the comparison result over sites Jornada_LTER and Santa_Rita.

Only less than 9% sites have a bias higher than ±0.05. The Cabauw site is in Netherlands and some of the albedo retrievals in winter time are from observations with larger-than-favorite SZA angle (>60°). The separated matchups with favorite SZA angles show a reduced bias to 0.0321. The other five sites are influenced by heterogeneity factor,

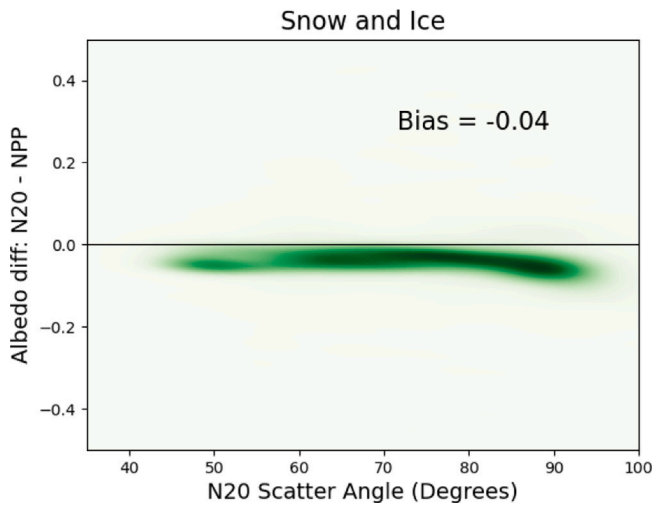


**Fig. 9.** Scatter density plot showing the variation of "NOAA-20 minus S-NPP" albedo difference with the NOAA-20 scattering angle over snow direct retrievals on Dec 30, 2019. The darker color represents higher density.

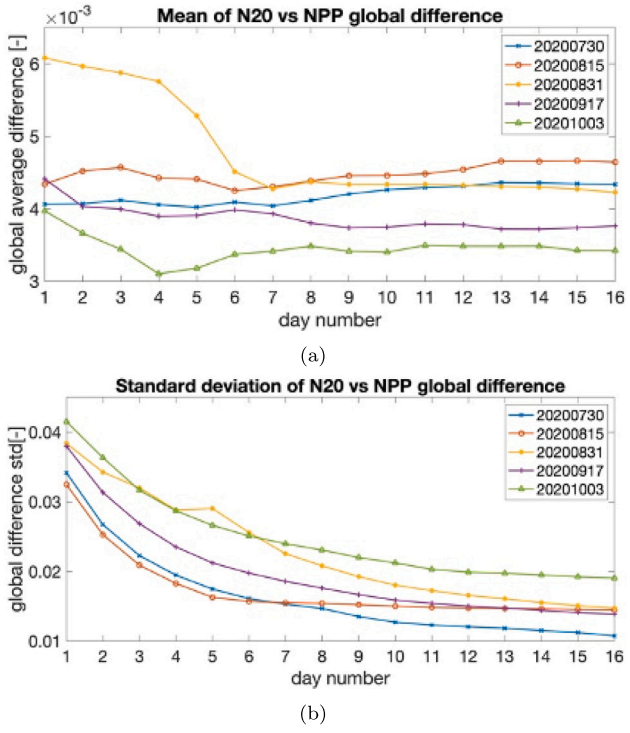


**Fig. 10.** Temporal plot showing the mean (left) and standard deviation (right) of the albedo difference between NOAA-20 and S-NPP over direct retrievals over the globe from the date noted in the legend.

especially at two urban sites, Budapest and Tateno, as well as the site Toravere near a residential area. In addition, two sites reveal the increased uncertainty due to the terrain effect, including the site Lower_Teakettle and the Wind_River, because the BRDF is modified as well as the sun and view angles on the surface by the micro-area topography (Wen et al., 2013). For the desert LUT, this factor corresponds to the bare soil type in land cover data (DeFries et al., 1995), and the VIIRS albedo shows an over-estimation and scattered error compared to in-situ albedo. The represented site is Gobabeb. From the scale difference plot at this site, the albedo scale difference is in the same direction as the validation error, and the within-pixel standard deviation shows a substantial influence (Fig. 14). The VIIRS albedo retrieval over this desert site has a stable magnitude, but still with a bias relative to ground measurements. This implies that the desert albedo LUT needs more validation from the future ground measurements and the BRDF model for LUT retrieval may need to be further improved. It should be noted that this bias trend is highly similar and comparable to other albedo products such as EUMETSAT LSA-SAF and MCD43 (Lellouch et al., 2020).

The ice LUT was applied at Georg von site and the comparison reached an excellent agreement with a bias of 0.01 and std of 0.03 under clear-sky conditions.

Snow-covered matchups could be caught in the sites with larger albedo value ranging from low snow-free matchups to high snow matchups from seasonal variation, such as Boulder_CO, ARM sites, Dakota_Coteau, and et al.. This can be observed that the VIIRS snow albedo could generally match the ground measured albedo magnitude. For the snow surface, the impact of heterogeneity is more significant due to the uneven snow coverage between the around-instrument area and the larger-pixel-area coupled with the brighter snow surface. As shown in Fig. 14(a), the heterogeneity condition of each site in each month could be observed. It could be seen that the scale difference and within-pixel std are generally larger in winter months, leading to larger validation bias during this period. 14(b) implies the sites with more deviated validation bias (y-value) usually have larger within-pixel std. Both the validation bias and within-pixel std are largest in January and February.

## 5. Cross-comparison with MODIS

### 5.1. Comparison datasets

Fig. 15 shows the spatial mean value of MODIS BSA (black-sky albedo at local solar noon) and WSA (white-sky albedo) and the daily mean blue-sky albedo in different latitude zones to illustrate their difference in the validation case. The albedo magnitude varying trend with latitude conforms to the characteristics of surface-type features. Over mid and low latitudes from 50°S to 40°N where snow-free land dominates, the BSA near noon is the smallest albedo, while the WSA shows the largest value. However, the BSA could be the largest value among them at high latitudes. Moreover, the statistical results vary temporally.

One sample date, that is Feb 15, 2019, is used in the global comparison, covering different LUT types and quality groups. The S-NPP VIIRS and MODIS albedo maps are shown in Fig. 16. Considering the albedo feature under different LUT types, the comparisons are further illustrated over snow, bare soil, and generic land, respectively.

### 5.2. S-NPP VIIRS and MODIS albedo cross-comparison results

#### 5.2.1. Albedo over desert or bare soil region

For bare soil pixels, VIIRS albedo can reach high consistency with MODIS albedo with an essentially zero bias (Fig. 17). Some scattered matchups result in a RMSE of 0.02 when comparing with the best MODIS retrievals ($QF = 0$) and a RMSE of 0.03 when comparing with good MODIS retrievals ($QF = 1$). It is interesting to observe that VIIRS retrievals from large-angle observations demonstrate higher consistency with MODIS, indicating that large angle retrievals in the Direct Estimation Method may not be considered as degraded over bare-soil-covered surfaces. Thus, the BRDF samples used in LUT training have captured their strong forward-scattering characteristics.

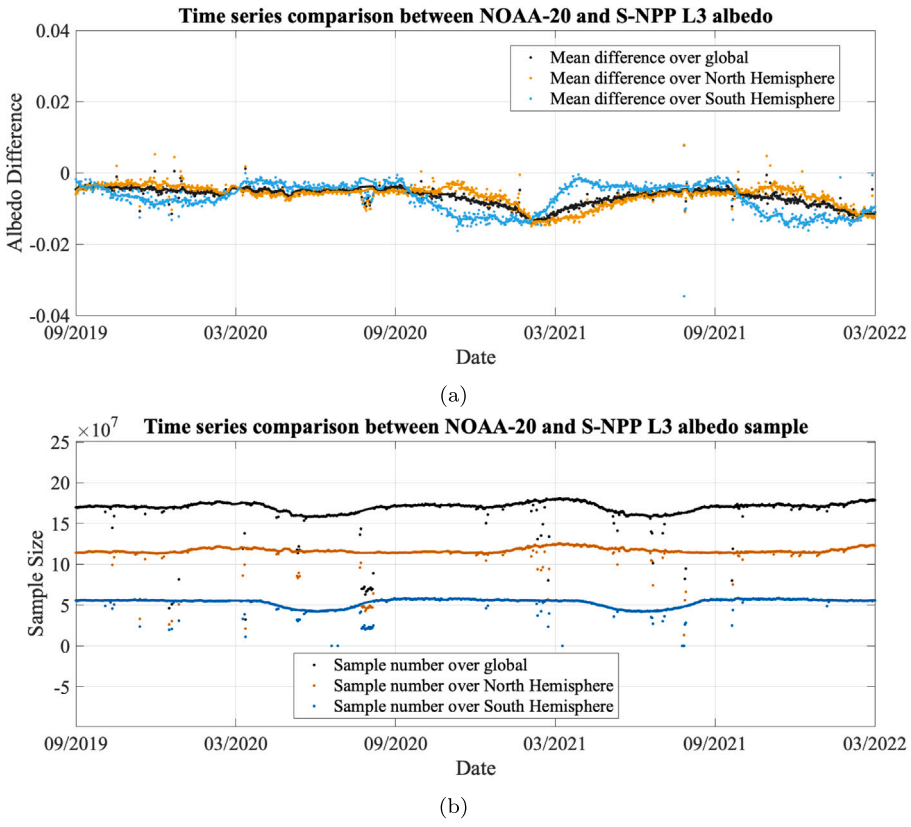


**Fig. 11.** The mean of difference between NOAA-20 and S-NPP albedo (a) and sample size (b) globally, over the Northern hemisphere, and over the southern hemisphere. Noted that the samples are subsets from every 5 × 5 pixels.

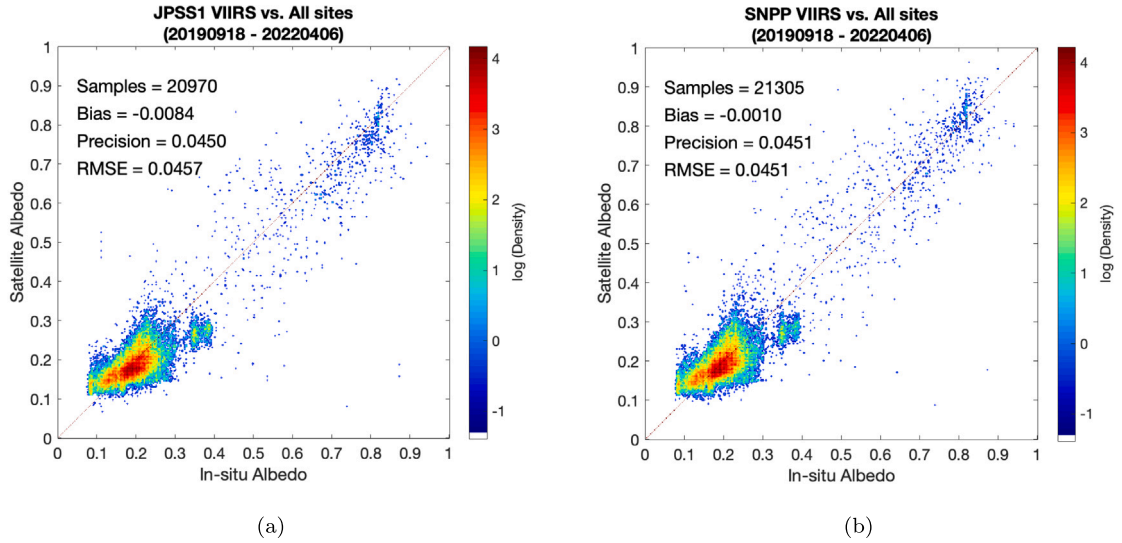


**Fig. 12.** Comparison of clear-sky albedo and in-situ daily mean albedo combined for all the sites. The solid line represents the zero error line. In-situ albedo with in-situ quality of 0 and 1 are shown (a) NOAA-20 (b) S-NPP VIIRS albedo.

### *5.2.2. Snow albedo*

Snow shows a unique BRDF feature (i.e., the forward-scattering nature under large solar incidence angles) (Wallner et al., 2017). In the MODIS albedo algorithm, snow observations are selected for BRDF modeling and NTB conversion if the pixel is regarded as snow. A snow-specific LUT is generated and used to derive snow albedo in the Direct Estimation Method (Qu et al., 2013; Wang et al., 2017). When the snow surface is recognized by the upstream snow cover, the albedo calculation of that pixel employs the snow-specific LUT, leading to the better performance on snow-covered pixels.

The VIIRS and MODIS albedos were compared in terms of the confidently snow surface; that is, the pixel is flagged as snow surface

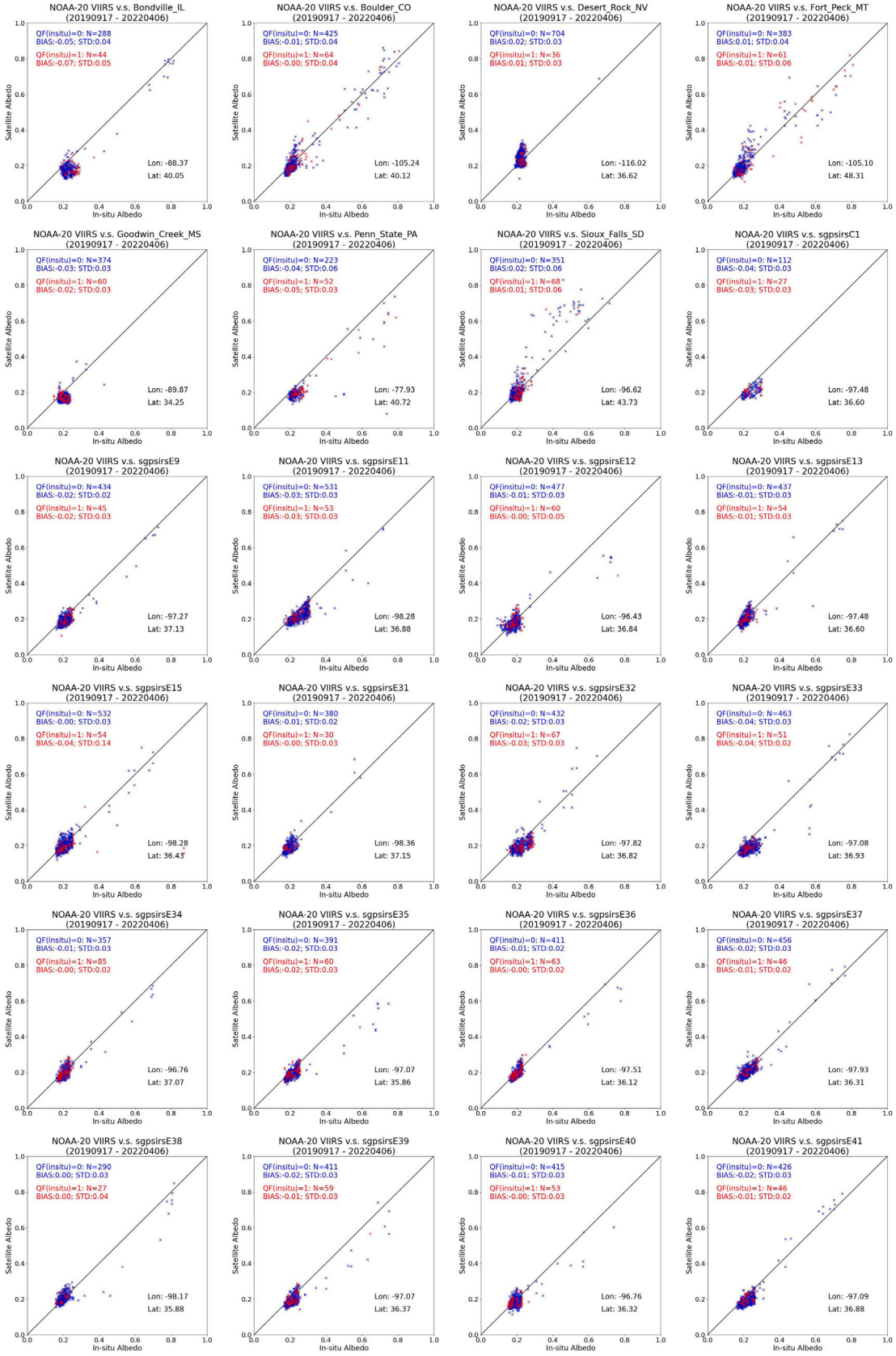


(a)

**Fig. 13.** Comparison between in-situ daily mean albedo and clear-sky NOAA-20 VIIRS albedo. A distinction is made between in-situ daily mean albedo with $DQF$ of 0 (blue) and 1 (red). The solid line represents the zero error line. (For interpretation of the references to color in this figure legend, the reader is referred to the web version of this article.)

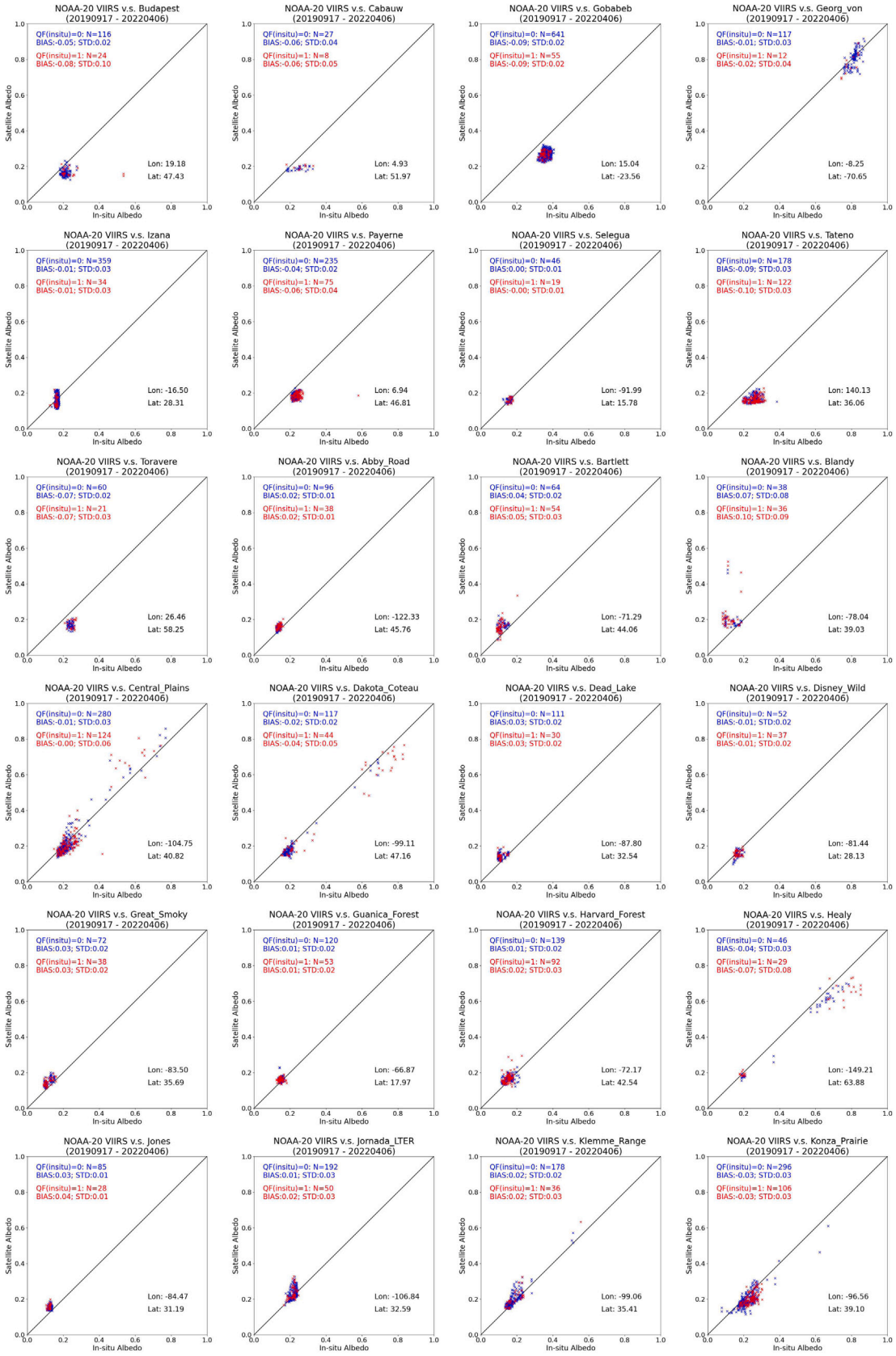


(b)

**Fig. 13.** (*continued*).

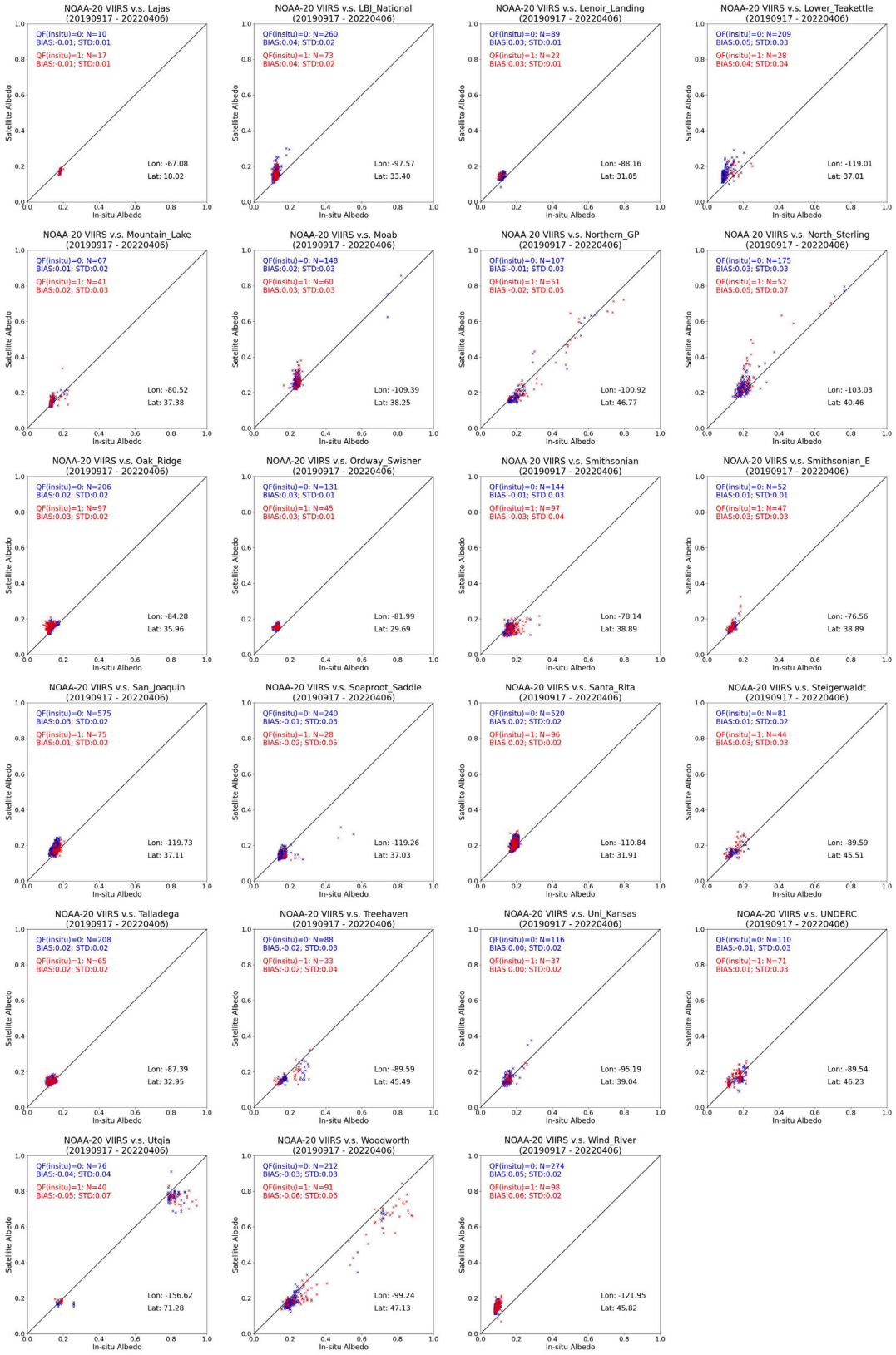


(c)

**Fig. 13.** (*continued*).

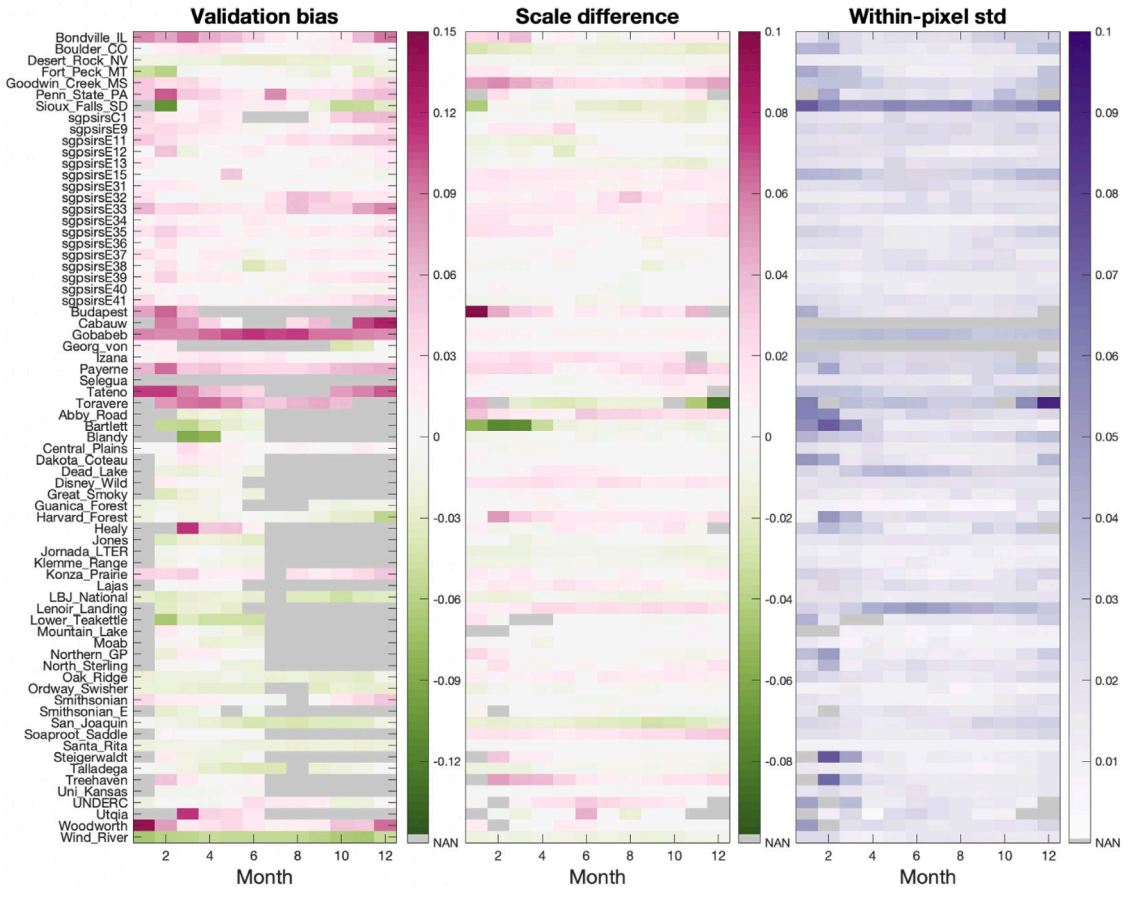


**Fig. 14.** The surface heterogeneity and validation error at each site in different seasons (monthly). (a) Images of the site-specific monthly validation bias (left) and heterogeneity related variables: scale difference (middle) and within-pixel std (right). In each image, one row for one site, and one column for one month. The color is a function of the variable value, and the correspondence is shown in the color bar. The BSRN and NEON sites have been integrated in the validation system for a shorter time and some seasons do not have valid clear-sky matchups yet, are masked as gray color. (b) Coupling of the monthly bias between monthly validation bias and the surface heterogeneity as the within-pixel std. The y-value of each dot represents the mean difference between VIIRS and ground measured albedos at one site in the month tie to the a-value. The color of each dot is a function of the within-pixel std as the correspondence shown in the color bar. (For interpretation of the references to color in this figure legend, the reader is referred to the web version of this article.)

in both products (Fig. 18). The snow surface observations mostly come with long oblique view path or large SZA values with larger inherent uncertainties in the observation. The VIIRS direct retrievals (with overall quality bit of 0 or 1) and MODIS full inversions (inversion quality of 0 or 1, as defined in the MCD43A2 product) are compared according to their overall quality in four mutually exclusive and exhaustive groups. The comparison between pixels with high quality in one product but only good quality in another product is also demonstrated for understanding its entire performance. The results show that their best retrievals (both quality of 0) generally agree (Fig. 18(a)). The VIIRS

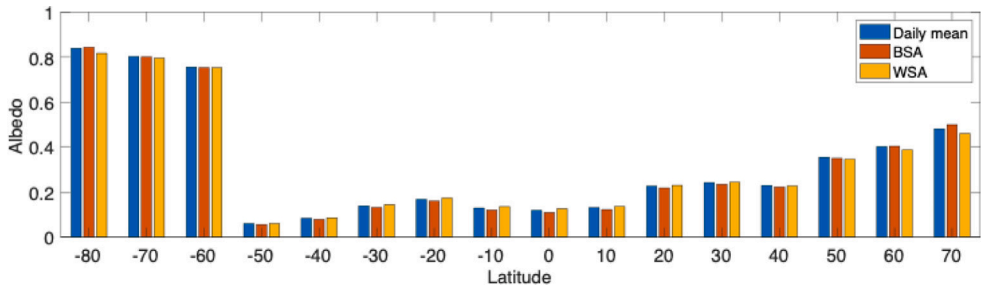


**Fig. 15.** Distribution of MODIS daily mean albedo calculated from MCD43A1 with BSA and WSA provided in MCD43A3 along with the latitude belts on Feb 15, 2019.

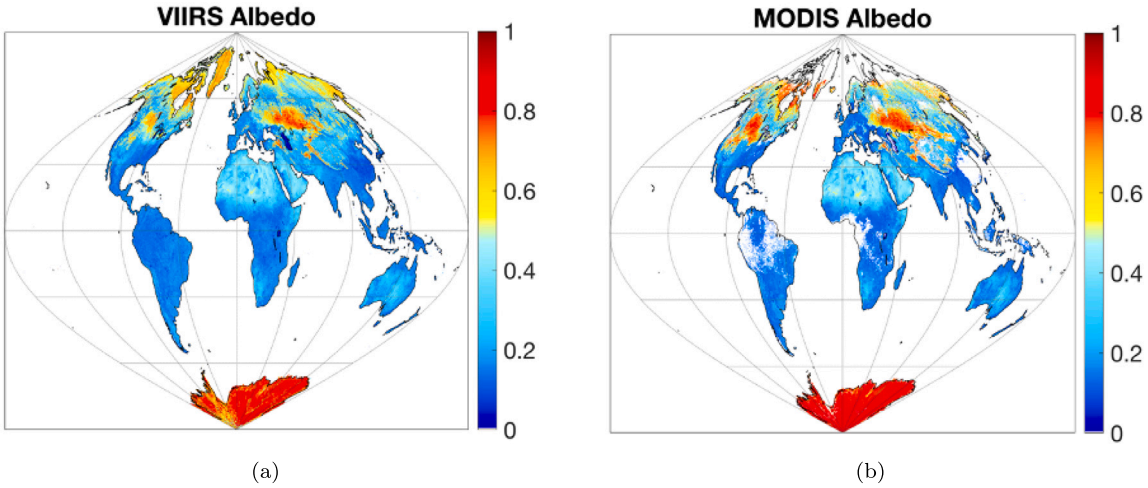


**Fig. 16.** The VIIRS and MODIS albedo dataset used in comparison.

shows slightly higher albedo at the high end, with a mean difference of 0.02. When the VIIRS direct retrieval using larger angles (quality of 1) is compared with the MODIS best quality retrievals (Fig. 18(b)), the overall agreement is excellent, but the inconsistency at the high end is magnified with a mean difference of 0.04, which is related to the VIIRS snow LUT inconsistency in different angular bins at larger VZA angles. Compared with the best quality VIIRS albedo, good-quality MODIS albedo is more scattered (Fig. 18(c)). A separate cluster of matchups appears at the high end for the same reason of VIIRS snow albedo angular inconsistency in Fig. 18(b). When we compare the both good-quality results of VIIRS and MODIS (Fig. 18(d)), the density scatterplot shows separate pixel clusters, which is related to different mean snow albedo in two hemispheres. For the VIIRS, the snow-specific LUT is adopted with more emphasis on the complete surface spectral information in LUT training rather than surface anisotropy (Wang et al., 2017). The next-step mitigations of VIIRS albedo on this issue will focus on the calibration of the separate regression relationships at different solar/view angle bins.

Fig. 19 shows the comparison results over matchups between VIIRS and MODIS with snow cover inconsistency. Note that the VIIRS LSA L3 algorithm has preserved all the snow retrievals in granular albedo as the snow albedo retrievals have the highest priority to be selected by the composition algorithm. Thus, the snow omission on L3 VIIRS albedo should be inherited from the upstream snow cover input. Fig. 19(b) show the influence of applying an incorrect, bare soil LUT to a snow surface, leading to a lower-than-normal albedo value over the Antarctic region. That is, the snow omission caused the misuse of LUT type, and thus degraded the accuracy of the albedo retrieval. The misuse of the bare-soil LUT for the snow surface is the main factor for the inconsistency in the polar region. The main reason for snow omission is snow-covered areas being confused with cloud cover and overestimation of cloud percentage. The VIIRS snow mask only provides valid retrieval over absolutely clear sky. When the cloud mask shows overestimation of cloud percentage over a bright surface such as snow, the absolutely clear pixels are largely suppressed to be probably clear and lose the opportunity of snow checking. This problem will be mitigated after a new surface-type marking the permanent snow is introduced.

Provided that the snow mask has recognized the snow, the VIIRS algorithm can estimate snow albedo through a single clear-sky observation with comparable accuracy as that of MODIS using a multi-day dataset, as discussed in Section 5.2. This provided the advantage of VIIRS albedo over fresh/new snow or temporal snow when MODIS albedo is limited by insufficient snow observations accumulated for BRDF modeling. The underestimation of MODIS albedo over snow surface is demonstrated in Fig. 19(c).

#### 5.2.3. Generic land pixels

In addition to the snow and bare soil LUTs, a generic LUT trained with all samples for various surface types and aerosol types is applied to all other land cases. There is a bias of 0.03 between the best VIIRS and MODIS retrievals in this group, showing a higher estimation from the VIIRS (Fig. 20). Given that in-situ validation has shown an underestimation by VIIRS albedo over vegetation-covered sites, this may indicate that S-NPP is closer to in-situ measurements, which requires further evaluation with the time-series dataset as planned.

Moreover, an evident vertical branch around MODIS albedo 0.2 existed between generic land VIIRS and snow-free MODIS albedos (Fig. 20(b)). The clustered and deviated pixels within the branch

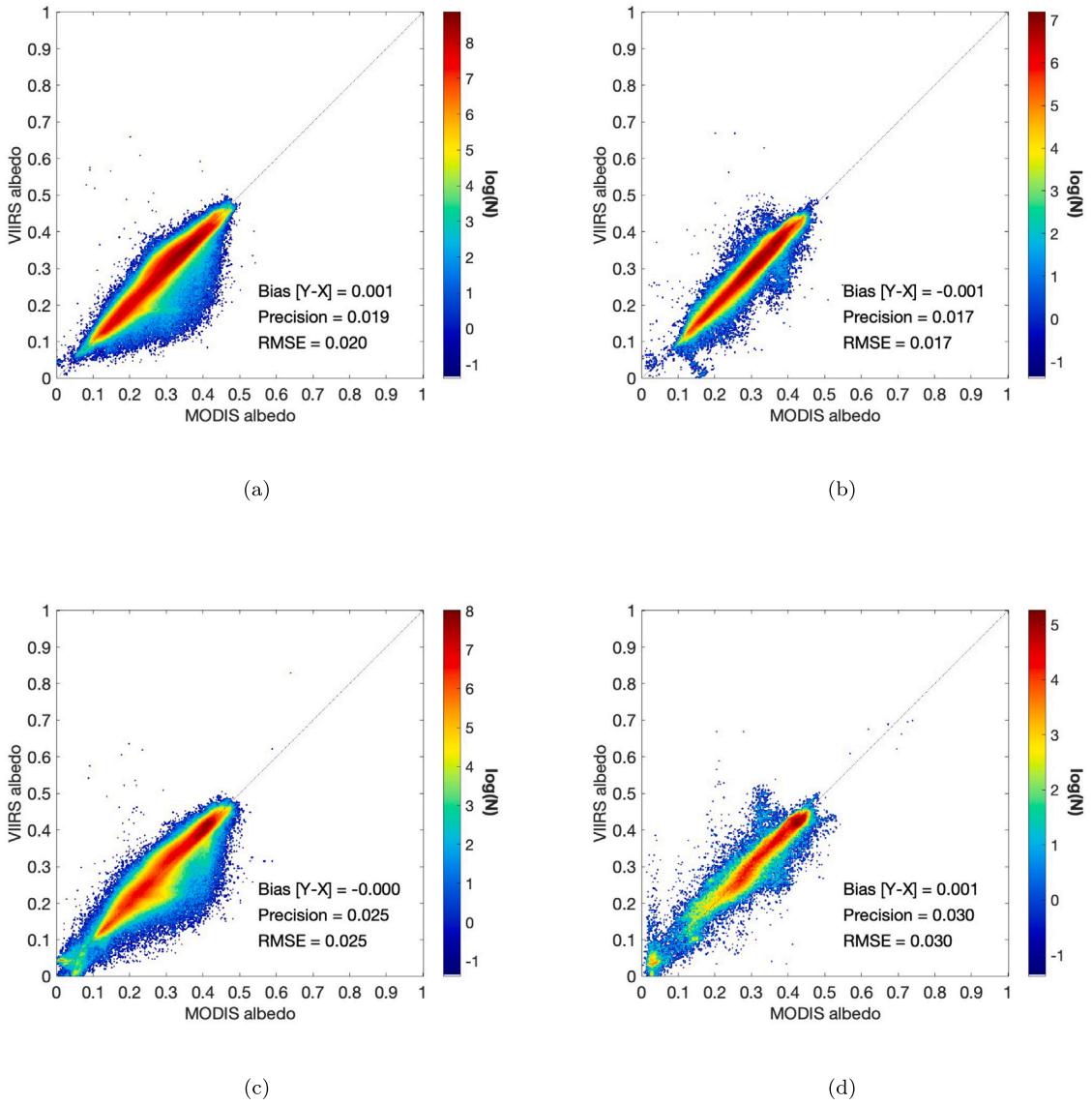


**Fig. 17.** Scatter density plot of VIIRS and MODIS albedo over bare soil pixels for different quality groups. (a) VIIRS best with MODIS best; (b) VIIRS good with MODIS best; (c) VIIRS best with MODIS good; (d) VIIRS good with MODIS good.

suggest higher VIIRS albedo than MODIS albedo, which agrees with Fig. 19(c). Fig. 21 shows the spatial distribution of the scattered points, which distribute over Europe and Asia, mainly at or around snow-covered regions based on the IMS snow map. This suggests that suspicious pixels are largely covered by snow. For the VIIRS algorithm, when the snow surface is retrieved using a generic land LUT due to omission of the snow cover input, it may cause an essentially zero mean error (Fig. 19(a)). However, for MODIS albedo, the pixel suffering from snow omission would only adopt snow-free observations for BRDF modeling and snow-free NTB coefficients, which would generate much lower albedo values. Thus, we can observe a magnitude difference between the VIIRS and MODIS albedos at these pixels.

## 6. Conclusions

The VIIRS albedo is an important EDR in the land product series of NOAA-20 and S-NPP. It is also in an active development phase for being better ingested to climate models. L3-gridded albedo is one milestone on the road toward a more user-friendly albedo product applicable in surface energy budget and climate change research. This study aimed to highlight the features and characterize the performance of L3 VIIRS albedo from both NOAA-20 and S-NPP as a function of L2 albedo, inputs of cloud, surface type, snow mask, and quality control screening. Resulting VIIRS albedo has fulfilled its first goal to be globally continuous and comparable to existing products while being produced in near-real time.

L3 VIIRS albedos from NOAA-20 and S-NPP have a high degree of global consistency, as expected because the same algorithm is applied. However, their daily comparison demonstrates a surface-type-dependent difference along the satellite orbit. For example, the generic vegetation difference is related to the SZA and VZA. The SZA-induced uncertainty is inherent in the LUT in the Direct Estimation Method, whereas the VZA-related uncertainty results from the pixel footprint difference. The albedo discrepancy over bare soil and snow shows a correlation with their strong forward scattering. The discrepancy between NOAA-20 and S-NPP is apparently reduced by aggregating albedo over time as the orbital difference has been counteracted. A long-term comparison between mean albedos globally suggests that retrievals from NOAA-20 and S-NPP are consistent. The mean albedo

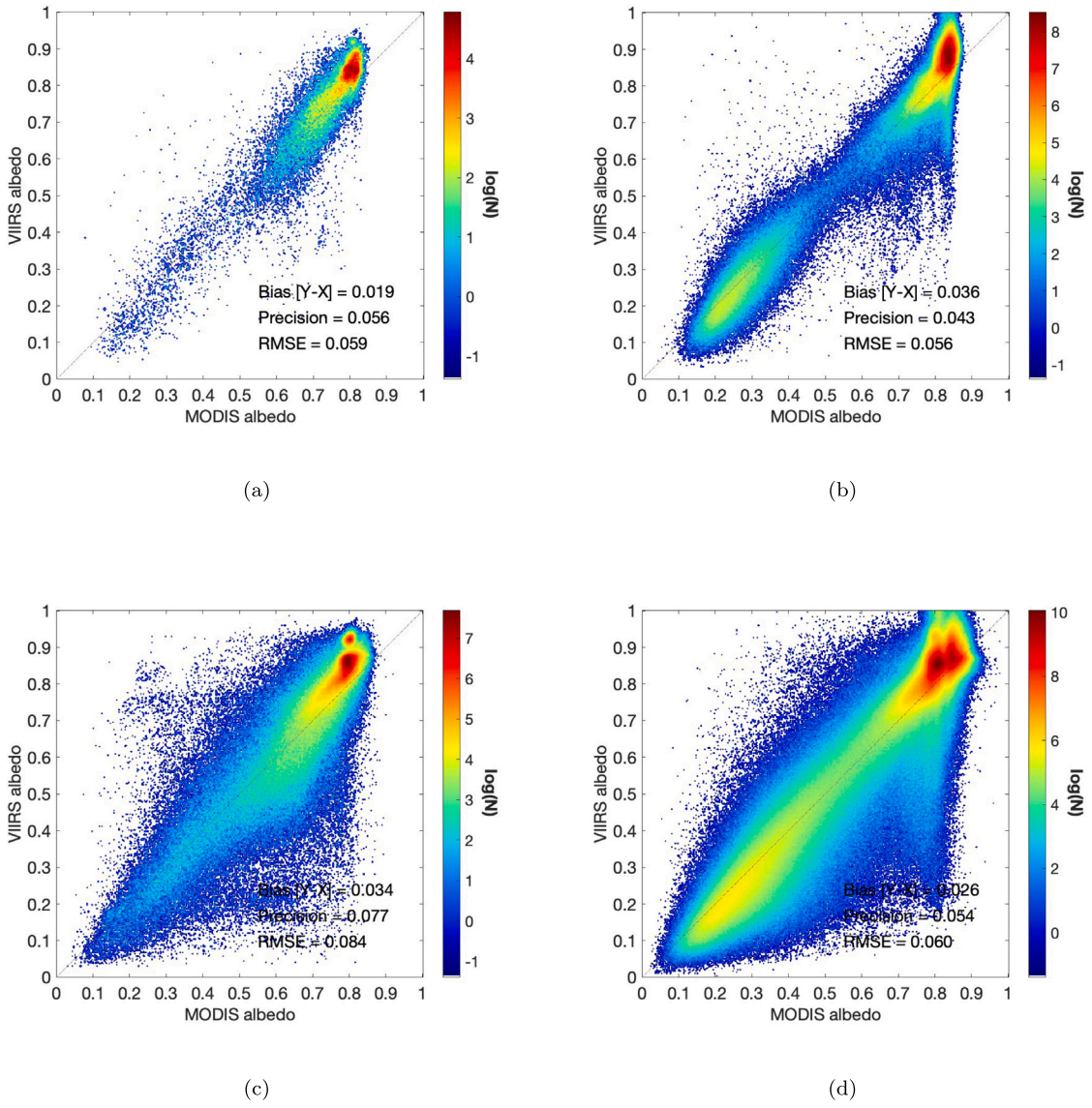


**Fig. 18.** Density scatter plot of VIIRS and MODIS albedo over snow pixels over different quality groups. (a) VIIRS best with MODIS best; (b) VIIRS good with MODIS best; (c) VIIRS best with MODIS good; (d) VIIRS good with MODIS good. Note that the red color represents higher density. (For interpretation of the references to color in this figure legend, the reader is referred to the web version of this article.)

difference over the southern hemisphere shows larger bias during the southern hemisphere summer due to snow cover omission.

In this study, VIIRS albedo was validated using a time series of in-situ counterparts collected from networks such as SURFRAD, BSRN, and ARM-SGP, due to their high reliability and timely data release. During the calculation of site daily mean albedo, we carefully considered the data quality and conducted instantaneous cloud screening based on downward shortwave radiation. According to the defined quality of in-situ daily mean albedo, the comparison was conducted on two groups of matchups with additional clear-sky measurements during daytime. Although the statistics meet the pre-defined requirements, a reduction of its bias and precision is expected with future algorithm refinements. The source of bias is partially from the surface heterogeneity according to the assessment result of the scale difference using 30-m Landsat 8 albedo retrievals. The value of precision reveals noise in the direct retrievals; this can be attributed to the algorithm assuming that the atmospheric conditions at the overpass time can represent the daily average condition. Long-term evaluation of the algorithm suggests that the retrieval satisfies the pre-defined albedo accuracy requirements.

To assess the product performance globally, we conducted cross-comparisons between the VIIRS and MODIS daily mean albedos over various retrieval paths at a resolution of 1 km. VIIRS albedo shows high agreement with MODIS albedo over desert, snow surface with same snow mask, and most generic land surfaces. The consistency between VIIRS and MODIS albedos appears limited for suspicious snow surface around the edge of snow coverage. Clearly, the VIIRS albedo algorithm is capable of capturing temporal new snow with a single observation. However, when apparent snow omission occurs over Greenland or the Antarctic region, albedo underestimation is observed due to the use of the bare soil LUT, rather than the one for permanent snow surface. The comparison demonstrates the importance of snow mask completeness to albedo quality. Switching the snow mask input from the current dataset to IMS is an ongoing effort in the operational system.

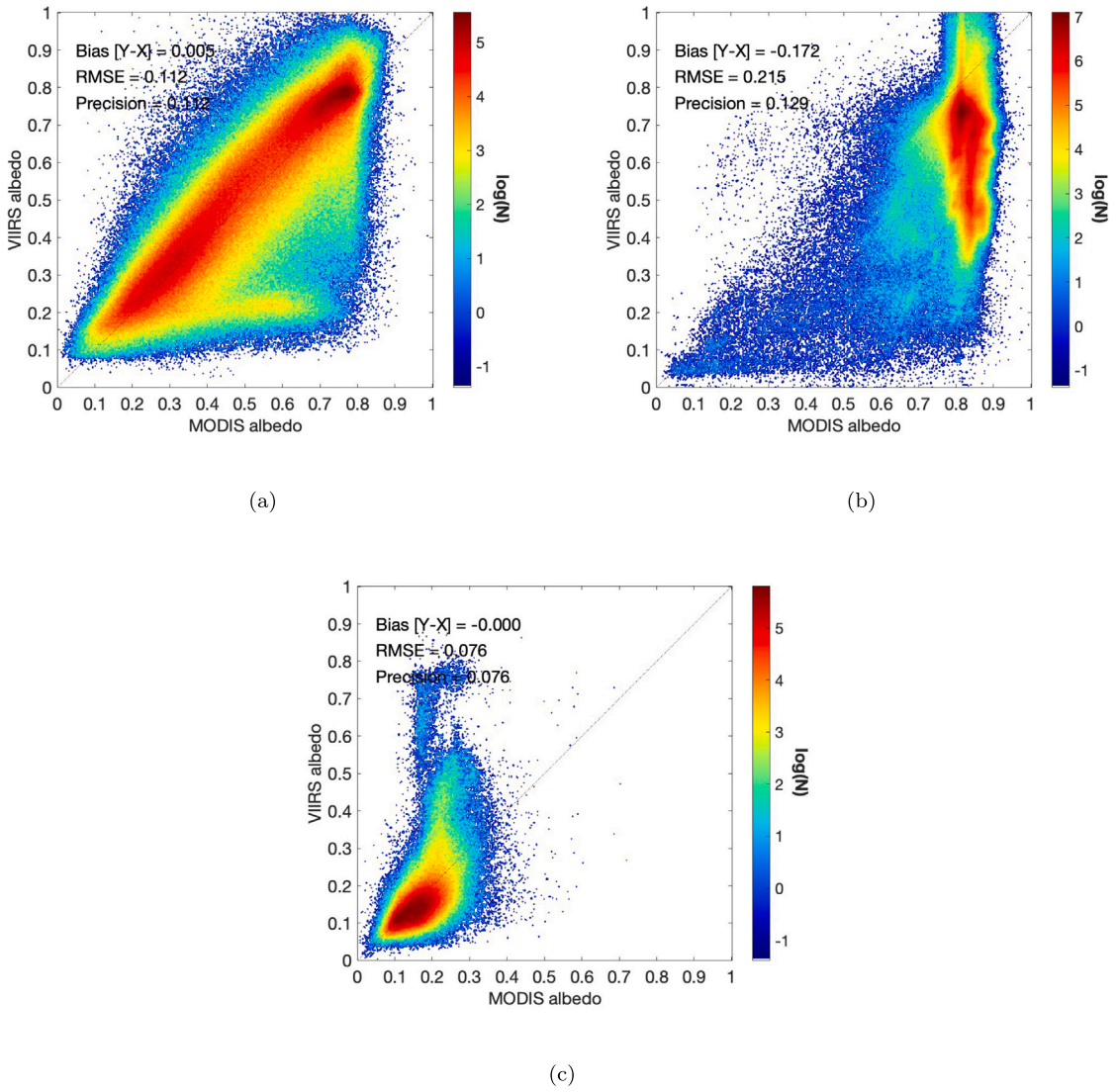


**Fig. 19.** (a) VIIRS generic, while MODIS snow; (b) VIIRS bare soil while MODIS snow; (c) VIIRS snow while MODIS snow-free.

Generally, the evaluation results show that the VIIRS global land surface albedo product can offer complete spatial coverage, with a retrieval bias mostly comparable to existing state-of-the-art albedo and BRDF-integrated albedo from multi-day observations, and it can better capture the snow albedo dynamic. Although the LUTs of this algorithm have good performance, some discrepancy has been observed over bright surface (deserts and snow). This suggests a need for further refinement of the input snow mask data. Others to be considered include the inherent uncertainty of radiance correction (Peng et al., 2018) and the simplified assumption of a stable atmospheric and surface condition in the Direct Estimation Method (Schueler et al., 2002). The introduced method can be easily adapted to other sensors, such as the future EPS-SG METImage (Wallner et al., 2017). Furthermore, it is anticipated that a merged global gridded VIIRS albedo dataset, comprising data from both NOAA-20 and S-NPP L2 albedo granules, would demonstrate enhanced quality and long-term stability.

## CRediT authorship contribution statement

**Jingjing Peng:** Conceptualization, Methodology, Software, Validation, Formal analysis, Investigation, Visualization, Product algorithm and validation software, Writing – original draft, Reviewing & editing. **Peng Yu:** Validation system software, Visualization, Writing – review & editing. **Yunyue Yu:** Conceptualization, Supervision, Writing – review & editing. **Aolin Jia:** Investigation. **Dongdong Wang:** Product algorithm software. **Heshun Wang:** Product algorithm software. **Zhihao Wang:** Data curation.

## Declaration of competing interest

The authors declare that they have no known competing financial interests or personal relationships that could have appeared to influence the work reported in this paper.

## Data availability

Data will be made available on request.

## Acknowledgments

This study was supported by National Oceanic and Atmospheric Administration, United States of America grant NA19NES4320002 (Cooperative Institute for Satellite Earth System Studies—CISESS) at the University of Maryland/ESSIC. The manuscript contents are solely the opinions of the authors and do not constitute a statement of policy, decision, or position on behalf of NOAA or the U. S. Government.

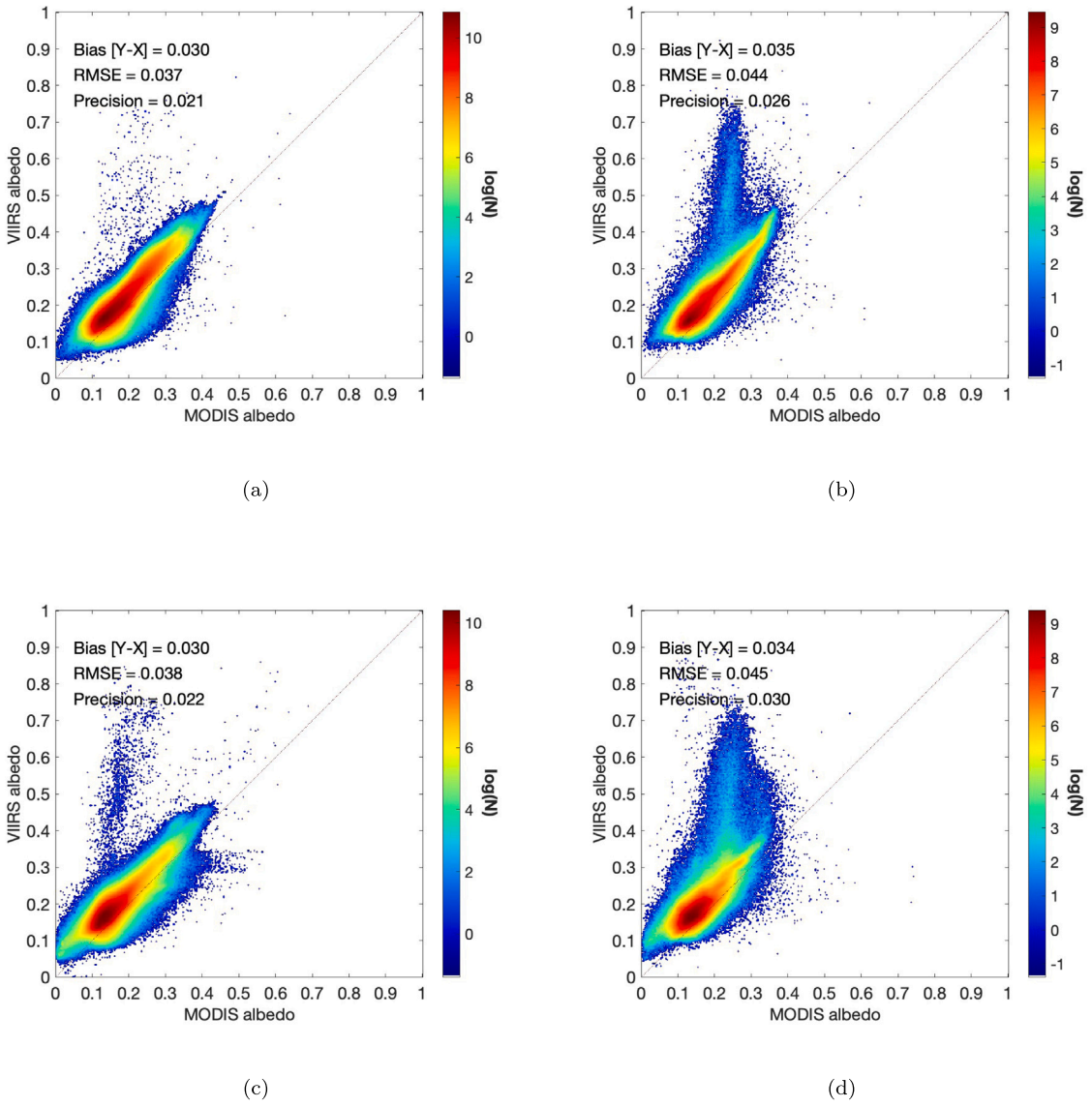


**Fig. 20.** Density plot of VIIRS and MODIS albedo over generic pixels among different quality groups. (a) VIIRS best with MODIS best; (b) VIIRS good with MODIS best; (c) VIIRS best with MODIS good; (d) VIIRS good with MODIS good.

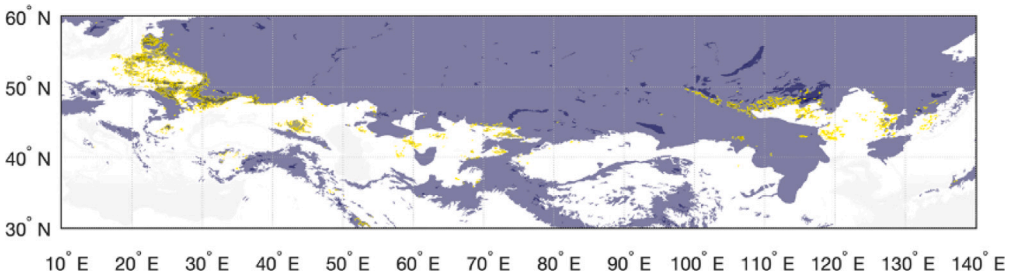


**Fig. 21.** Distribution of the inconsistent points (yellow) overlapped on IMS snow cover data (gray blue) with the VIIRS albedo coverage as background (light gray). The inland water covered grids are shown in dark blue, and the sea-water covered grids are in white. (For interpretation of the references to color in this figure legend, the reader is referred to the web version of this article.)

## References

Abraha, M., Chen, J., Hamilton, S.K., Sciusco, P., Lei, C., Shirkey, G., Yuan, J., Robertson, G.P., 2021. Albedo-induced global warming impact of conservation reserve program grasslands converted to annual and perennial bioenergy crops. Environ. Res. Lett. 16 (8), 084059.

Alkama, R., Cescatti, A., 2016. Biophysical climate impacts of recent changes in global forest cover. Science 351 (6273), 600–604.

Augustine, J.A., Hodges, G.B., Cornwall, C.R., Michalsky, J.J., Medina, C.I., 2005. An update on SURFRAD—The GCOS surface radiation budget network for the continental United States. J. Atmos. Ocean. Technol. 22 (10), 1460–1472.

Cao, C., Blonski, S., Wang, W., Uprety, S., Shao, X., Choi, J., Lynch, E., Kalluri, S., 2018. NOAA-20 VIIRS on-orbit performance, data quality, and operational Cal/Val support. In: Earth Observing Missions and Sensors: Development, Implementation, and Characterization V, Vol. 10781. International Society for Optics and Photonics, 107810K.

Cao, C., Xiong, J., Blonski, S., Liu, Q., Uprety, S., Shao, X., Bai, Y., Weng, F., 2013. Suomi NPP VIIRS sensor data record verification, validation, and long-term performance monitoring. J. Geophys. Res.: Atmos. 118 (20), 11–664.

Chapin, F.S., Sturm, M., Serreze, M.C., McFadden, J.P., Key, J.R., Lloyd, A.H., McGuire, A.D., Rupp, T.S., Lynch, A.H., Schimel, J.P., 2005. Role of land-surface changes in arctic summer warming. Science 310 (5748), 657–660.

Chapin, III, F.S., Randerson, J.T., McGuire, A.D., Foley, J.A., Field, C.B., 2008. Changing feedbacks in the climate–biosphere system. Front. Ecol. Environ. 6 (6), 313–320.

Chiu, J., Paredes-Mesa, S., Lakhankar, T., Romanov, P., Krakauer, N., Khanbilvardi, R., Ferraro, R., 2020. Intercomparison and validation of MIRS, MSPPS, and IMS snow cover products. Adv. Meteorol. 2020.

DeFries, R., Hansen, M., Townshend, J., 1995. Global discrimination of land cover types from metrics derived from AVHRR pathfinder data. Remote Sens. Environ. 54 (3), 209–222.

Driemel, A., Augustine, J., Behrens, K., Colle, S., Cox, C., Cuevas-Agulló, E., Denn, F.M., Duprat, T., Fukuda, M., Grobe, H., 2018a. Baseline surface radiation network (BSRN): structure and data description (1992–2017). Earth Syst. Sci. Data 10 (3), 1491–1501.

Driemel, A., Augustine, J., Behrens, K., Colle, S., Cox, C., Cuevas-Agulló, E., Denn, F.M., Duprat, T., Fukuda, M., Grobe, H., et al., 2018b. Baseline surface radiation network (BSRN): structure and data description (1992–2017). Earth Syst. Sci. Data 10 (3), 1491–1501.

Fletcher, C.G., Thackeray, C.W., Burgers, T.M., 2015. Evaluating biases in simulated snow albedo feedback in two generations of climate models. J. Geophys. Res. 120 (1), 12–26. http://dx.doi.org/10.1002/2014JD022546.

Franch, B., Vermote, E.F., Claverie, M., 2014. Intercomparison of landsat albedo retrieval techniques and evaluation against in situ measurements across the US SURFRAD network. Remote Sens. Environ. 152, 627–637.

Gardner, A.S., Sharp, M.J., 2010. A review of snow and ice albedo and the development of a new physically based broadband albedo parameterization. http://dx.doi.org/10.1029/2009JF001444.

Gladkova, I., Ignatov, A., Shahriar, F., Kihai, Y., Hillger, D., Petrenko, B., 2016. Improved VIIRS and MODIS SST imagery. Remote Sens. 8 (1), 1–20. http://dx.doi.org/10.3390/rs8010079.

Gleeson, T., Moosdorf, N., Hartmann, J., van Beek, L.P.H., Crook, J.A., Forster, P.M., 2014. Comparison of surface albedo feedback in climate models and observations. Geophys. Res. Lett. 41 (5), 1717–1723. http://dx.doi.org/10.1002/2014GL061184. Received.

Grant, I.F., Prata, A.J., Cechet, R.P., 2000. The impact of the diurnal variation of albedo on the remote sensing of the daily mean albedo of grassland. J. Appl. Meteorol. 39 (2), 231–244.

Greuell, W., Oerlemans, J., 2004. Narrowband-to-broadband albedo conversion for glacier ice and snow: Equations based on modeling and ranges of validity of the equations. Remote Sens. Environ. 89 (1), 95–105. http://dx.doi.org/10.1016/j.rse.2003.10.010.

Helfrich, S.R., McNamara, D., Ramsay, B.H., Baldwin, T., Kasheta, T., 2007. Enhancements to, and forthcoming developments in the interactive multisensor snow and ice mapping system (IMS). Hydrol. Process.: Int. J. 21 (12), 1576–1586.

Hillger, D., Kopp, T., Lee, T., Lindsey, D., Seaman, C., Miller, S., Solbrig, J., Kidder, S., Bachmeier, S., Jasmin, T., 2013. First-light imagery from suomi NPP VIIRS. Bull. Am. Meteorol. Soc. 94 (7), 1019–1029.

Hillger, D., Line, W.E., Seaman, C., Miller, S.D., Finley, S., Kopp, T.J., 2022. Ten years of VIIRS EDR imagery validation and user interactions. Remote Sens. 14 (17), 4167.

Jacob, F., Olioso, A., 2005. Derivation of diurnal courses of albedo and reflected solar irradiance from airborne POLDER data acquired near solar noon. J. Geophys. Res.: Atmos. 110 (D10).

Jia, A., Wang, D., Liang, S., Peng, J., Yu, Y., 2022. Global daily actual and snow-free blue-sky land surface albedo climatology from 20-year MODIS products. J. Geophys. Res.: Atmos. e2021JD035987.

Jin, Y., Schaaf, C.B., Woodcock, C.E., Gao, F., Li, X., Strahler, A.H., Lucht, W., Liang, S., 2003. Consistency of MODIS surface bidirectional reflectance distribution function and albedo retrievals: 2. Validation. J. Geophys. Res.: Atmos. 108 (D5).

Justice, C.O., Román, M.O., Csiszar, I., Vermote, E.F., Wolfe, R.E., Hook, S.J., Friedl, M., Wang, Z., Schaaf, C.B., Miura, T., 2013. Land and cryosphere products from suomi NPP VIIRS: Overview and status. J. Geophys. Res.: Atmos. 118 (17), 9753–9765.

Khlopenkov, K.V., Trishchenko, A.P., 2008. Implementation and evaluation of concurrent gradient search method for reprojection of MODIS level 1B imagery. IEEE Trans. Geosci. Remote Sens. 46 (7), 2016–2027.

Knorr, W., Schnitzler, K.G., 2006. Enhanced albedo feedback in north Africa from possible combined vegetation and soil-formation processes. Clim. Dynam. 26 (1), 55–63. http://dx.doi.org/10.1007/s00382-005-0073-9.

Kucharski, F., Zeng, N., Kalnay, E., 2013. A further assessment of vegetation feedback on decadal Sahel rainfall variability. Clim. Dynam. 40 (5–6), 1453–1466. http://dx.doi.org/10.1007/s00382-012-1397-x.

Kumar, S., Mocko, D., Vuyovich, C., Peters-Lidard, C., 2020. Impact of surface albedo assimilation on snow estimation. Remote Sens. 12 (4), http://dx.doi.org/10.3390/rs12040645.

Lee, X., Goulden, M.L., Hollinger, D.Y., Barr, A., Black, T.A., Bohrer, G., Bracho, R., Drake, B., Goldstein, A., Gu, L., et al., 2011. Observed increase in local cooling effect of deforestation at higher latitudes. Nature 479 (7373), 384–387.

Lellouch, G., Carrer, D., Vincent, C., Pardé, M., C Frietas, S., Trigo, I.F., 2020. Evaluation of two global land surface albedo datasets distributed by the copernicus climate change service and the EUMETSAT LSA-SAF. Remote Sens. 12 (11), 1888.

Li, Z., Erb, A., Sun, Q., Liu, Y., Shuai, Y., Wang, Z., Boucher, P., Schaaf, C., 2018. Preliminary assessment of 20-m surface albedo retrievals from sentinel-2A surface reflectance and MODIS / VIIRS surface anisotropy measures. Remote Sens. Environ. 217 (August), 352–365. http://dx.doi.org/10.1016/j.rse.2018.08.025, URL: https://doi.org/10.1016/j.rse.2018.08.025.

Liang, S., 2001. Narrowband to broadband conversions of land surface albedo I: Algorithms. Remote Sens. Environ. 76 (2), 213–238.

Liang, S., Stroeve, J., Box, J.E., 2005a. Mapping daily snow/ice shortwave broadband albedo from moderate resolution imaging spectroradiometer (MODIS): The improved direct retrieval algorithm and validation with greenland in situ measurement. J. Geophys. Res. D: Atmosp. 110 (10), 1–10. http://dx.doi.org/10.1029/2004JD005493.

Liang, S., Wang, D., He, T., Yu, Y., 2019. Remote sensing of earth's energy budget: Synthesis and review. Int. J. Digit. Earth 12 (7), 737–780.

Liang, S., Wang, D., Zhou, Y., Yu, Y., Peng, J., 2018. Algorithm theoretical basis document for gridded VIIRS land surface temperature and albedo production. URL: https://www.star.nesdis.noaa.gov/jpss/documents/ATBD/ATBD_EPS_Land_SurfaceAlbedo_v1.3.pdf, Last accessed 22 September 2022.

Liang, S., Yu, Y., Defelice, T.P., 2005b. VIIRS narrowband to broadband land surface albedo conversion: Formula and validation. Int. J. Remote Sens. 26 (5), 1019–1025. http://dx.doi.org/10.1080/01431160512331340156.

Liu, N., Liu, Q., Wang, L., Liang, S., Wen, J.G., Qu, Y., Liu, S., 2013a. A statistics-based temporal filter algorithm to map spatiotemporally continuous shortwave albedo from MODIS data. Hydrol. Earth Syst. Sci. 17 (6), 2121.

Liu, J., Schaaf, C., Strahler, A., Jiao, Z., Shuai, Y., Zhang, Q., Roman, M., Augustine, J.A., Dutton, E.G., 2009a. Validation of moderate resolution imaging spectroradiometer (MODIS) albedo retrieval algorithm: Dependence of albedo on solar zenith angle. J. Geophys. Res.: Atmos. 114 (1), 1–11. http://dx.doi.org/10.1029/2008JD009969.

Liu, J., Schaaf, C., Strahler, A., Jiao, Z., Shuai, Y., Zhang, Q., Roman, M., Augustine, J.A., Dutton, E.G., 2009b. Validation of moderate resolution imaging spectroradiometer (MODIS) albedo retrieval algorithm: Dependence of albedo on solar zenith angle. J. Geophys. Res.: Atmos. 114 (D1).

Liu, Q., Wang, L., Qu, Y., Liu, N., Liu, S., Tang, H., Liang, S., 2013b. Preliminary evaluation of the long-term GLASS albedo product. Int. J. Digit. Earth 6 (sup1), 69–95.

Lucht, W., 1998. Expected retrieval accuracies of bidirectional reflectance and albedo from EOS-MODIS and MISR angular sampling. J. Geophys. Res.: Atmos. 103 (D8), 8763–8778.

Lucht, W., Roujean, J.-L., 2000. Considerations in the parametric modeling of BRDF and albedo from multiangular satellite sensor observations. Remote Sens. Rev. 18 (2–4), 343–379.

Metzger, S., Ayres, E., Durden, D., Florian, C., Lee, R., Lunch, C., Luo, H., Pingintha-Durden, N., Roberti, J.A., SanClements, M., et al., 2019. From NEON field sites to data portal: a community resource for surface–atmosphere research comes online. Bull. Am. Meteorol. Soc. 100 (11), 2305–2325.

Minnis, P., Mayor, S., Smith, W.L., Young, D.F., 1997. Asymmetry in the diurnal variation of surface albedo. IEEE Trans. Geosci. Remote Sens. 35 (4), 879–890.

Moustafa, S.E., Rennermalm, A.K., Román, M.O., Wang, Z., Schaaf, C.B., Smith, L.C., Koenig, L.S., Erb, A., 2017. Evaluation of satellite remote sensing albedo retrievals over the ablation area of the southwestern greenland ice sheet. Remote Sens. Environ. 198, 115–125. http://dx.doi.org/10.1016/j.rse.2017.05.030.

NOAA, NASA, 2015. Joint polar satellite system (JPSS) operational algorithm description (OAD) document for gridding/granulation (G/G) and VIIRS gridded intermediate products (GIP) software.

Peng, J., Yu, P., Yu, Y., 2019a. NOAA VIIRS albedo long-term-monitoring webpage. URL: https://www.star.nesdis.noaa.gov/smcd/emb/land/animation.php?sat=JPSS1&product=LSA, Last accessed 22 September 2022.

Peng, J., Yu, P., Yu, Y., 2019b. NOAA VIIRS albedo long-term-validation webpage. URL: https://www.star.nesdis.noaa.gov/smcd/emb/land/validation.php?sat=JPSS1&product=LSA&network=All, Last accessed 22 September 2022.

Peng, J., Yu, Y., Yu, P., Liang, S., 2018. The VIIRS sea-ice albedo product generation and preliminary validation. Remote Sens. 10 (11), http://dx.doi.org/10.3390/rs10111826.

Pitman, A., Avila, F., Abramowitz, G., Wang, Y., Phipps, S., de Noblet-Ducoudré, N., 2011. Importance of background climate in determining impact of land-cover change on regional climate. Nature Clim. Change 1 (9), 472–475.

Potter, S., Solvik, K., Erb, A., Goetz, S.J., Johnstone, J.F., Mack, M.C., Randerson, J.T., Román, M.O., Schaaf, C.L., Turetsky, M.R., Veraverbeke, S., Walker, X.J., Wang, Z., Massey, R., Rogers, B.M., 2020. Climate change decreases the cooling effect from postfire albedo in boreal north America. Global Change Biol. 26 (3), 1592–1607. http://dx.doi.org/10.1111/gcb.14888.

Qu, Y., Liang, S., Liu, Q., He, T., Liu, S., Li, X., 2015. Mapping surface broadband albedo from satellite observations: A review of literatures on algorithms and products. Remote Sens. 7 (1), 990–1020.

Qu, Y., Liu, Q., Liang, S., Wang, L., Liu, N., Liu, S., 2013. Direct-estimation algorithm for mapping daily land-surface broadband albedo from MODIS data. IEEE Trans. Geosci. Remote Sens. 52 (2), 907–919.

Ramsay, B.H., 1998. The interactive multisensor snow and ice mapping system. Hydrol. Process. 12 (10–11), 1537–1546.
Remund, J., Wald, L., Lefèvre, M., Ranchin, T., Page, J.H., 2003. Worldwide linke turbidity information. In: ISES Solar World Congress 2003, Vol. 400. International Solar Energy Society (ISES), p. 13.
Riihelä, A., Manninen, T., Laine, V., Andersson, K., Kaspar, F., 2013. CLARA-SAL: A global 28 yr timeseries of earth's black-sky surface albedo. Atmos. Chem. Phys. 13 (7), 3743–3762. http://dx.doi.org/10.5194/acp-13-3743-2013.
Roman, M.O., Gatebe, C.K., Shuai, Y., Wang, Z., Gao, F., Masek, J.G., He, T., Liang, S., Schaaf, C.B., 2013. Use of in situ and airborne multiangle data to assess MODIS- and landsat-based estimates of directional reflectance and albedo. IEEE Trans. Geosci. Remote Sens. 51 (3), 1393–1404. http://dx.doi.org/10.1109/TGRS.2013.2243457.
Román, M.O., Schaaf, C.B., Lewis, P., Gao, F., Anderson, G.P., Privette, J.L., Strahler, A.H., Woodcock, C.E., Barnsley, M., 2010. Assessing the coupling between surface albedo derived from MODIS and the fraction of diffuse skylight over spatially-characterized landscapes. Remote Sens. Environ. 114 (4), 738–760.
Schaaf, C.B., Gao, F., Strahler, A.H., Lucht, W., Li, X., Tsang, T., Strugnell, N.C., Zhang, X., Jin, Y., Muller, J.-P., 2002. First operational BRDF, albedo nadir reflectance products from MODIS. Remote Sens. Environ. 83 (1–2), 135–148.
Schaepman-Strub, G., Schaepman, M.E., Painter, T.H., Dangel, S., Martonchik, J.V., 2006. Reflectance quantities in optical remote sensing—Definitions and case studies. Remote Sens. Environ. 103 (1), 27–42.
Schueler, C.F., Clement, J.E., Ardanuy, P.E., Welsch, C., DeLuccia, F., Swenson, H., 2002. NPOESS VIIRS sensor design overview. In: Earth Observing Systems VI, Vol. 4483. International Society for Optics and Photonics, pp. 11–23.
Song, R., Muller, J.-P., Kharbouche, S., Woodgate, W., 2019. Intercomparison of surface albedo retrievals from MISR, MODIS, CGLS using tower and upscaled tower measurements. Remote Sens. 11 (6), 644.
Stokes, G.M., Schwartz, S.E., 1994. The atmospheric radiation measurement (ARM) program: Programmatic background and design of the cloud and radiation test bed. Bull. Am. Meteorol. Soc. 75 (7), 1201–1222.
Stroeve, J.C., Box, J.E., Fowler, C., Haran, T., Key, J., 2001. Intercomparison between in situ and AVHRR polar pathfinder-derived surface albedo over greenland. Remote Sens. Environ. 75 (3), 360–374. http://dx.doi.org/10.1016/S0034-4257(00)00179-6.
Stroeve, J., Box, J.E., Wang, Z., Schaaf, C., Barrett, A., 2013. Re-evaluation of MODIS MCD43 greenland albedo accuracy and trends. Remote Sens. Environ. 138, 199–214. http://dx.doi.org/10.1016/j.rse.2013.07.023.
Uprety, S., Cao, C., Blonski, S., Shao, X., 2018. Evaluating NOAA-20 and S-NPP VIIRS radiometric consistency. In: Earth Observing Missions and Sensors: Development, Implementation, and Characterization V, Vol. 10781. International Society for Optics and Photonics, 107810V.
Wald, L., 2018. Basics in solar radiation at earth surface.
Wallner, O., Reinert, T., Straif, C., 2017. METIMAGE: a spectro-radiometer for the VII mission onboard METOP-SG. In: International Conference on Space Optics—ICSO 2016, Vol. 10562. International Society for Optics and Photonics, 105620E.
Wang, K., Augustine, J., Dickinson, R.E., 2012a. Critical assessment of surface incident solar radiation observations collected by SURFRAD, USCRN and AmeriFlux networks from 1995 to 2011. J. Geophys. Res.: Atmos. 117 (D23).
Wang, L., Cole, J.N.S., Bartlett, P., Verseghy, D., Derksen, C., Brown, R., von Salzen, K., Salzen, K., 2016a. Investigating the spread in surface albedo for snow-covered forests in CMIP5 models. J. Geophys. Res.: Atmos. 121 (3), 1104–1119. http://dx.doi.org/10.1002/2015JD023824.Received.
Wang, Z., Erb, A.M., Schaaf, C.B., Sun, Q., Liu, Y., Yang, Y., Shuai, Y., Casey, K.A., Román, M.O., 2016b. Early spring post-fire snow albedo dynamics in high latitude boreal forests using landsat-8 OLI data. Remote Sens. Environ. 185, 71–83.
Wang, D., Liang, S., He, T., Yu, Y., 2013. Direct estimation of land surface albedo from VIIRS data: Algorithm improvement and preliminary validation. J. Geophys. Res.: Atmos. 118 (22), 12–577.
Wang, D., Liang, S., He, T., Yu, Y., Schaaf, C., Wang, Z., Albedo, S., Viirs, F., 2015. Estimating daily mean land surface albedo from MODIS data. J. Geophys. Res.: Atmos. 120 (10), 4825–4841.
Wang, D., Liang, S., Zhou, Y., He, T., Yu, Y., Schaaf, C., Wang, Z., 2017. A new method for retrieving daily land surface albedo from VIIRS data. IEEE Trans. Geosci. Remote Sens. 55 (3), 1765–1775. http://dx.doi.org/10.1002/2015JD023178.Received.
Wang, Z., Schaaf, C.B., Chopping, M.J., Strahler, A.H., Wang, J., Román, M.O., Rocha, A.V., Woodcock, C.E., Shuai, Y., 2012b. Evaluation of moderate-resolution imaging spectroradiometer (MODIS) snow albedo product (MCD43a) over tundra. Remote Sens. Environ. 117, 264–280. http://dx.doi.org/10.1016/j.rse.2011.10.002.
Wang, Z., Schaaf, C.B., Strahler, A.H., Chopping, M.J., Román, M.O., Shuai, Y., Woodcock, C.E., Hollinger, D.Y., Fitzjarrald, D.R., 2014. Evaluation of MODIS albedo product (MCD43a) over grassland, agriculture and forest surface types during dormant and snow-covered periods. Remote Sens. Environ. 140, 60–77. http://dx.doi.org/10.1016/j.rse.2013.08.025.
Wang, Z., Schaaf, C., Sun, Q., Shuai, Y., Román, M., 2018a. Capturing rapid land surface dynamics with collection V006 MODIS BRDF/NBAR/Albedo (MCD43) products. Journal 207, http://dx.doi.org/10.1016/j.rse.2018.02.001.
Wang, Z., Schaaf, C.B., Sun, Q., Shuai, Y., Román, M.O., 2018b. Capturing rapid land surface dynamics with collection V006 MODIS BRDF/NBAR/Albedo (MCD43) products. Remote Sens. Environ. 207, 50–64.
Wen, J., Zhao, X., Liu, Q., Tang, Y., Dou, B., 2013. An improved land-surface albedo algorithm with DEM in rugged terrain. IEEE Geosci. Remote Sens. Lett. 11 (4), 883–887.
Wolfe, R.E., Roy, D.P., Vermote, E., 1998. MODIS Land Data Storage, Gridding, and Compositing Methodology: Level 2 Grid. Technical Report 4.
Wu, X., Wen, J., Xiao, Q., Yu, Y., You, D., Hueni, A., 2017. Assessment of NPP VIIRS albedo over heterogeneous crop land in northern China. J. Geophys. Res.: Atmos. 122 (24), 13–138.
Wu, X., Xiao, Q., Wen, J., Liu, Q., Peng, J., Li, X., 2014. Advances in uncertainty analysis for the validation of remote sensing products: Take leaf area index for example. Yaogan Xuebao/J. Remote Sens. 18 (5), http://dx.doi.org/10.11834/jrs.20143332.
Yu, Y., Liu, Y., Peng, J., Wang, H., Yu, P., 2019a. Algorithm theoretical basis document for gridded VIIRS land surface temperature and albedo production. URL: https://www.star.nesdis.noaa.gov/jpss/documents/ATBD/ATBD_Gridded_VIIRS_LST_LSA_v1.pdf, Last accessed 22 September 2022.
Yu, Y., Peng, J., Yu, P., 2019b. NOAA VIIRS albedo long-term-validation web-page. URL: https://www.star.nesdis.noaa.gov/smcd/emb/land/validation.php?sat=JPSS1&product=LSA&network=All, Last accessed 22 September 2022.
Zhou, L., Dickinson, R.E., Tian, Y., Vose, R.S., Dai, Y., 2007. Impact of vegetation removal and soil aridation on diurnal temperature range in a semiarid region: Application to the Sahel. Proc. Natl. Acad. Sci. 104 (46), 17937–17942.
Zhou, Y., Wang, D., Liang, S., Yu, Y., He, T., 2016. Assessment of the suomi NPP VIIRS land surface albedo data using station measurements and high-resolution albedo maps. Remote Sens. 8 (2), 137.
Zhu, Z., Wang, S., Woodcock, C.E., 2015. Improvement and expansion of the fmask algorithm: Cloud, cloud shadow, and snow detection for landsats 4–7, 8, and sentinel 2 images. Remote Sens. Environ. 159, 269–277.